MICROCOPY RESOLUTION TEST CHART
NATIONAL BUREAU OF STANDARDS-1963-A

LEVEL

Automatic Target Hand-Off For Non-Compatible Imaging Systems

by

J. S. Boland, III, L. J. Pinson, and E. G. Peters

Electrical Engineering Department
Auburn University
Auburn, Alabama 36830

ENGINEERING EXPERIMENT STATION
Auburn University
Auburn, Alabama 36830

15 September 1978

79 03 06 036

AUTOMATIC TARGET HAND-OFF FOR

NON-COMPATIBLE IMAGING SYSTEMS

by

J. S. Boland, III, L. J. Pinson, and E. G. Peters

Electrical Engineering Department
Auburn University
Auburn, Alabama   36830

Final Technical Report
For the Period 20 July 1977 - 15 September 1978

ENGINEERING EXPERIMENT STATION
Auburn University
Auburn, Alabama   36830

15 September 1978

79 03 06 036

REPORT DOCUMENTATION PAGE		READ INSTRUCTIONS BEFORE COMPLETING FORM
1. REPORT NUMBER	2. GOVT ACCESSION NO.	3. RECIPIENT'S CATALOG NUMBER
4. TITLE (and Subtitle) AUTOMATIC TARGET HAND-OFF FOR NON-COMPATIBLE IMAGING SYSTEMS,		5. TYPE OF REPORT & PERIOD COVERED Final Technical Report. 20 July 1977 - 15 Sep 1978
		6. PERFORMING ORG. REPORT NUMBER
7. AUTHOR(s) J. S. Boland, III, L. J. Pinson and E. G. Peters		8. CONTRACT OR GRANT NUMBER(s) DAAK40-77-C-0156
9. PERFORMING ORGANIZATION NAME AND ADDRESS Engineering Experiment Station Auburn University Auburn, AL 36830		10. PROGRAM ELEMENT, PROJECT, TASK AREA & WORK UNIT NUMBERS
11. CONTROLLING OFFICE NAME AND ADDRESS Commander, US Army Missile R. & D Command ATTN: DRDMI-TGC Redstone Arsenal, AL 35809		12. REPORT DATE 15 September 1978
		13. NUMBER OF PAGES 115
14. MONITORING AGENCY NAME & ADDRESS(If different from Controlling Office) 116 P'		15. SECURITY CLASS. (of this report) UNCLASSIFIED
		15a. DECLASSIFICATION/DOWNGRADING SCHEDULE

16. DISTRIBUTION STATEMENT (of this Report)

Cleared for Public Release; Distribution Unlimited

17. DISTRIBUTION STATEMENT (of the abstract entered in Block 20, if different from Report)

18. SUPPLEMENTARY NOTES

19. KEY WORDS (Continue on reverse side if necessary and identify by block number)

Correlation, Target Hand-Off, Image Correlation, Edge Detection

20. ABSTRACT (Continue on reverse side if necessary and identify by block number)

The problem of automatic hand-off of a target from a precision pointing and tracking system (PTS) to an imaging missile seeker using non-compatible imaging systems is considered in this report. The approach taken is to develop preprocessing algorithms which transform the input video signals to a compatible format for input to a binary correlation system.

The types of imaging systems considered are a high resolution day TV PTS for target acquisition and a low resolution Infra-Red Imaging Seeker (IRIS) for

DD FORM 1473 1 JAN 73   EDITION OF 1 NOV 65 IS OBSOLETE

402 958

the missile system. The approach taken is to study the effects on the correlation system of a number of preprocessing algorithms so that trade-offs of each can be presented. The results of implementing the preprocessing algorithms in a correlation system simulation are given and explained. The effects of differing sensor characteristics on the correlation function and the acceptance/rejection threshold are given. A preprocessing algorithm using edge detection is chosen and the advantages and disadvantages are listed.

ACCESSION for
NTIS   White Section
DDC   Buff Section
UNANNOUNCED
JUSTIFICATION

BY
DISTRIBUTION/AVAILABILITY CODES
Dist.   AVAIL and/or SPECIAL

TABLE OF CONTENTS

TABLE OF CONTENTS (Con't)

2
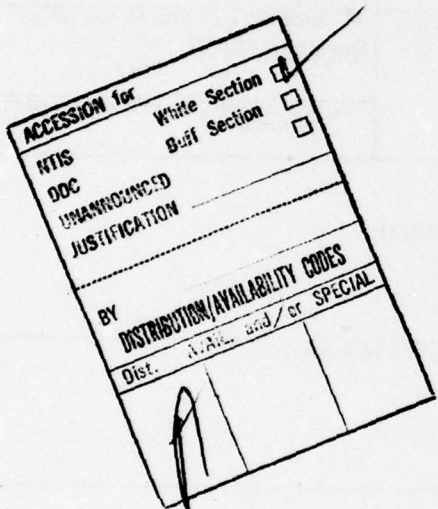
LIST OF FIGURES

3

LIST OF TABLES

5

1. INTRODUCTION

Currently the U.S. Army is developing a system for the acquisition, tracking, and laser designation of military targets from helicopters. The Army is testing a system which will accomplish automatic hand-off of targets when both imaging devices are day TV systems. Very little attention has been given to date to the problem of hand-off of a target when one or both of the imaging devices are active in different spectra. As a result the U.S. Army Research and Development Command, Huntsville, Alabama let a contract with the Engineering Experiment Station, Auburn University to study and make a recommendation for a system to accomplish automatic hand-off of targets from designators to imaging missile seekers when the imaging devices are dissimilar. This report presents the results of that effort.

A. Scope of Work

The purpose of this study is to analyze the complexity of hardware and software required to implement an automatic correlation technique to be used in "handing off" a target from a target acquisition device to an imaging missile seeker (IRIS). The function of an automatic correlator is to compare the video signals from the PTS and the missile seeker and to generate error signals to cause the missile seeker to slew such that its aimpoint coincides with that of the pointing and tracking unit. The work shall use as a starting point or basis the results obtained under contract DAAH01-76-C-0396 and reported in [4]. Specifically the

7

above final report recommended a correlator implementation for hand-off from a day TV PTS to a day TV seeker system. The scope of work performed under this contract was to extend the above results such that automatic hand-off of targets from a day TV or a Forward Looking Infra-Red (FLIR) system to an Infra-Red Imaging Seeker (IRIS) can be accomplished. The scope of work as written in the contract is given in the following five paragraphs for completeness.

The first phase shall be an investigation to determine as many techniques as possible for preprocessing the two images obtained from sensors with different characteristics such that hand-off can be accomplished using the correlator developed in contract DAAH01-76-C-0396. The emphasis shall be on preprocessing to make the new algorithm compatible with the existing correlator rather than a complete new design for a correlator.

The purpose of a preprocessing algorithm is to convert the signals from the two image sensors to a compatible form such that correlation can be accomplished. The preprocessing must correct for differing fields of view (FOV), aspect ratios, frame rates, interlacing, number of lines per TV frame, signal sampling rates, and sensor characteristics. Sensor characteristics are divided into differing spatial and spectral responses. Spatial differences are a result of the detectors used in each sensor. For example a FLIR may have a detector array or a single scanned detector while standard TV has a scanned electron beam. Spectral differences are a result of the detectors being sensitive in different frequency ranges such as in the visible spectrum and the IR spectrum.

Phase Two, which will actually be conducted concurrently with Phase One, shall consist of an investigation of the hardware and software needed

for various combinations of PTS and missile seeker head configurations. Consideration shall be given to differing characteristics as outlined above. The contractors shall consider various combinations and recommend the hardware and software necessary to implement each.

Phase Three shall consist of the actual analysis of complexity of the hardware/software necessary to implement the various combinations of Phase Two. This analysis shall be presented in such a way that MIRADCOM will be able to use it to make a trade-off of the various options available.

In Phase Four a preprocessing technique, along with the system constraints, shall be chosen in concert with the MIRADCOM technical director. This decision will be based on the results of the first three phases. The hardware and software to implement this approach shall be completely specified, and the preprocessing algorithm shall be developed.

B. Organization of Report

All of the work outlined in the Scope of Work has been completed and is documented in this final report. Chapter two formulates the preprocessing algorithms investigated. The preprocessing algorithms given in Chapter two convert the video signals received from the imaging system to a digitized binary signal based on the measures of average value, standard deviation, or edge content.

Chapter three outlines a correlation system simulation program used to study the preprocessors given in Chapter two. The results of a number of simulations are presented and explained in Chapter three. The results presented in Chapter three satisfy task three of the scope of work.

Two subjects are treated in Chapter four. First a descriptive review of the imaging sensor characteristics is given in terms of typical performance parameters and their interrelationships. Secondly, further analysis of threshold statistics for the binary correlator is given which seeks to place the analysis on a more sound theoretical base and to include the very real possibility of pixel mis-match at registration due to sensor contrast reversals or geometric distortions. A continuation of previous work is presented for completeness which allows for inclusion of pixel mis-match.

Chapter five gives the conclusions and recommendations resulting from the above work in fulfillment of task five of the scope of work. Questions which arose during the course of this work but were not answered due to lack of time or lack of simulation facilities are also given.

2. FORMULATION OF PREPROCESSING ALGORITHMS
USED TO FORM BINARY IMAGES

In this chapter many preprocessing algorithms are presented which can be used to transform the video images to a binary form for input to the correlation process. The algorithms discussed in sections A and B are applicable to a correlator system in which both images are acquired with sensors sensitive in the visual spectrum. The algorithms discussed in section C are applicable to a correlator system in which the HR image is acquired through a standard TV system and the seeker image is acquired with an infrared imaging seeker (IRIS).

A. Quantization Threshold Based on Average Value

To quantize the input video signals to one-bit (2-level) requires that a threshold value be set such that all signal levels above and equal to the threshold value become 1 and all signal levels below the threshold value become zero. One possible way to set the threshold is on the average value of the signal. This section explains two procedures of calculating the average signal value. Both methods are forms of a varying local average. This is done so that real time operation can be achieved.

1. Line Average Quantizer

Consider a single line of video as given in Figure 1. The pixel to

11

be quantized is X(i, j). The line average quantizer quantizes the points of the selected input array by calculating the average value of a specified number of previous pixel values of the same line. The quantization threshold is then this average value. Equation 1
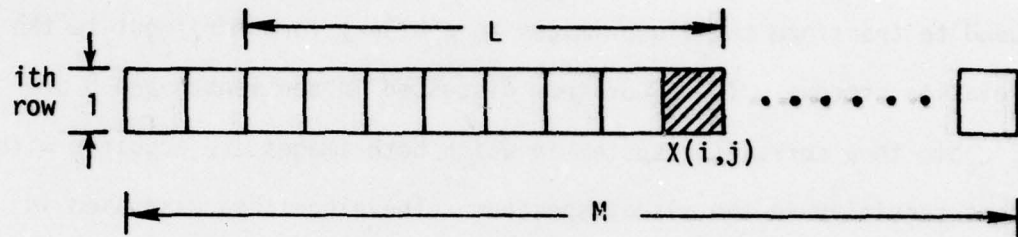
Figure 1. Layout for quantization based on a line average.

describes the average value calculation where L is the average value sample length.

$$\overline{X}(i,j) = \frac{1}{L} \sum_{J=1}^{L} X(i, j - J + 1) \tag{1}$$

Equation 2 gives the quantization process.

$$X_q(i,j) = \begin{cases} 1 & ; \quad X(i,j) \geq \overline{X}(i,j) \\ 0 & ; \quad X(i,j) < \overline{X}(i,j) \end{cases} \tag{2}$$

where $X_q(\cdot,\cdot)$ = quantized pixel.

This process would continue until all pixels in the input array are quantized. As can be seen from Figure 1, the first (L - 1) pixels of each video line will be quantized incorrectly and must be ignored in the correlation process. If the original input array is of size N x M, then the quantized array will contain N x (M - L + 1) valid points.

2. Array Average Quantizer

Consider the layout of the input video array as given in Figure 2. The pixel to be quantized is now located in the center of a K x L
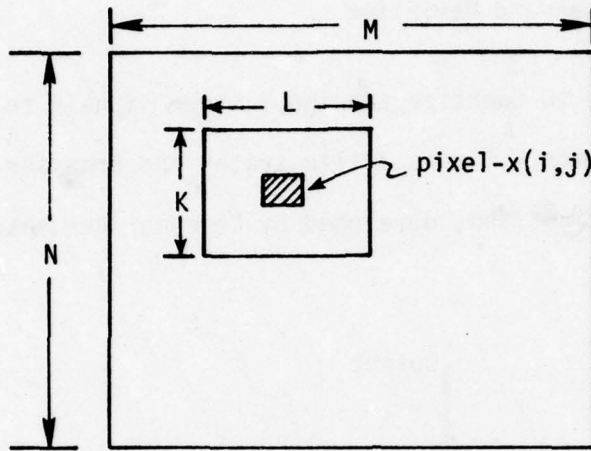
Figure 2. Layout of input array for quantization based on an array average.

subarray of pixel values. The average value used for the threshold is now based on the average value of the K x L pixel subarray. Equation 3 details the average value calculation.

$$\overline{X}(i,j) = \frac{1}{KL} \sum_{I=1}^{K}\sum_{J=1}^{L} X(i - k - 1 + I, j - \ell - 1 + J) \quad (3)$$

where, k = largest integer $\leq$ K/2

ℓ = largest integer $\leq$ L/2

The quantization process is given by Equation 2. As can be seen from Figure 2, there is a border region of the input array which will be quantized incorrectly. There will be an array of (N - K + 1) x (M - L + 1) valid points in the resulting quantized array. It should be noted that the array average quantization process requires intermediate storage of

[(K - 1)*M] + L pixel values of the input array whereas the line

average quantization process would require (L - 1) pixel values to be

saved.

B.   Quantization Threshold Based on Standard Deviation

A second method used to quantize the input video signals to one-bit

is explained in this section.   Figure 3 illustrates the transfer function

of the quantizer.   This algorithm, developed by Goodyear Aerospace Corporation,
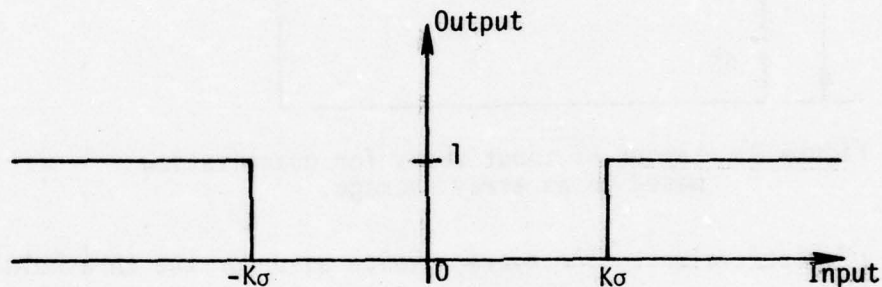
Figure 3.   Bilevel absolute value quantizer.

uses the absolute value of the live video and a threshold value proportional

to the standard deviation of the video signal to convert the live video

signal to a bilevel digitized array.   The application of the quantizer

shown in Figure 3 requires two calculations of the input video.   First,

the average value must be removed from the input video and second, the

standard deviation, σ, of the input video must be obtained so the

threshold, $K\sigma$, can be set.   The average value can be estimated by either

of the two algorithms given in part A.   This section explains two algo-

rithms used to estimate the standard deviation of the video signal.

1. Standard Deviation of a Line Sample

Consider a single video line as shown in Figure 1. The sample standard deviation at the (ith, jth) pixel based on a sample length L is given by Equation 4.

$$\sigma(i,j) = \left[\frac{1}{L} \sum_{J=1}^{L} \left\{ X(i,j-J+1) - \overline{X}(i,j) \right\}^2 \right]^{1/2} \qquad (4)$$

Then, expanding the term on the right yields

$$\sigma(i,j) = \left[\frac{1}{L} \sum_{J=1}^{L} \left\{ X^2(i,j-J+1) - 2\,X(i,j-J+1)\,\overline{X}(i,j) + \overline{X}^2(i,j) \right\} \right]^{1/2}$$

$$\sigma(i,j) = \left[\frac{1}{L} \left\{ \sum_{J=1}^{L} X^2(i,j-J+1) - 2\overline{X}(i,j) \sum_{J=1}^{L} X(i,j-J+1) + \overline{X}^2(i,j) \right\} \right]^{1/2} \qquad (5)$$

Substituting Equation 1 into 5 yields

$$\sigma(i,j) = \left[\frac{1}{L} \sum_{J=1}^{L} X^2(i,j-J+1) - \overline{X}^2(i,j) \right]^{1/2} \qquad (6)$$

The threshold value is proportional to the standard deviation calculated by Equation 6. Equation 7 gives the quantization process.

$$X_q(i,j) = \begin{cases} 1 & ; \; X(i,j) \geq K\sigma(i,j) + \overline{X}(i,j) \\ 0 & ; \; \overline{X}(i,j) - K\sigma(i,j) < X(i,j) < K\sigma(i,j) + \overline{X}(i,j) \\ 1 & ; \; X(i,j) \leq \overline{X}(i,j) - K\sigma(i,j) \end{cases} \qquad (7)$$

K, given in Equation 7, is a positive proportionality constant which would have to be known a-priori.

2. Standard Deviation of an Array Sample

Consider the K x L array sample of the input video as shown in Figure 2. The sample standard deviation based on the K x L subarray is given by Equation 8.

$$\sigma(i,j) = \left[\frac{1}{KL} \sum_{I=1}^{K} \sum_{J=1}^{L} \left\{ X(i-k-1+I, \ j-\ell-1+J) - \bar{X}(i,j) \right\}^2 \right]^{1/2} \quad (8)$$

where $X(i,j)$, k, and ℓ are given by Equation 3. Then, expanding the term on the right yields,

$$\sigma(i,j) = \left[\frac{1}{KL} \sum_{I=1}^{K} \sum_{J=1}^{L} X^2(i-k-1+I, \ j- \ell-1+J) - \bar{X}^2(i,j) \right]^{1/2} \quad (9)$$

The quantization process would again be given as in Equation (7).

C. Quantization Threshold Based on Edge Content

In order for the correlation of binary images to be a valid measure of similarity it is necessary that the quantization process be based on similar measures of scene content. For the case in which the images are obtained from sensors operating in different frequency spectrums, quantization based on average value or standard deviation no longer supplies similar binary images to the correlation system. Therefore, some other measure on which quantization is based must be used when correlating images from dissimilar sensors. One such measure investigated in this contract is that of edge content in the two images. All edge detection schemes base their decision on the gradient value associated with a particular pixel

in the image. Pixels exhibiting a high gradient value as compared with a threshold are considered to be edge points and those pixels with low gradient value are considered non-edge points.

This section explains two edge detection algorithms that could be implemented as a preprocessing step in the correlation system. The algorithms are basically two different ways to estimate the gradient magnitude at a particular pixel of interest with no preference given to direction of the gradient. It should be noted that both methods require selection of a gradient threshold to form binary images. The problem of selecting a proper gradient threshold will be addressed in a later chapter.

1. 2 x 2 Edge Detector

The method of edge detection presented here is known as the Roberts Cross Operator [1]. This method is based on the principle of estimating and selecting areas, in the digital picture, of high gradient activity. Figure 4 is the pixel representation of a 2 x 2 area in the digital picture. If the digital picture is represented by the two-dimensional function $g(x,y)$, then the magnitude of the gradient at pixel (i,j) can be approximated by Equation 10. From Equation 10 it can be seen
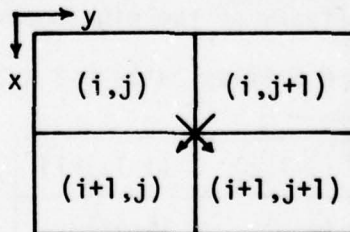
Figure 4. Pixel representation for the Roberts cross operator.

$$||\nabla g(i,j)|| \approx R(i,j) = \{[g(i,j) - g(i+1,j+1)]^2 + [g(i,j+1) - g(i+1,j)]^2\}^{1/2} \qquad (10)$$

that in picture areas of constant grey level, $R(i,j)$ will be zero and in picture areas of high grey level change in either the X or Y or both directions, $R(i,j)$ will be large. A more computationally efficient algorithm is given in Equation 11. $F(i,j)$ behaves very much like $R(i,j)$.

$$F(i,j) = |g(i,j) - g(i+1,j+1)| + |g(i,j+1) - g(i+1,j)| \quad (11)$$

To implement binary quantization using the gradient properties of Equation 11 necessitates the selection of a gradient threshold for values of $F(x,y)$. The quantization process is given in Equation 12, where $F_q(\cdot,\cdot)$ is the quantized gradient array and GTH the gradient threshold. The

$$F_q(i,j) = \begin{cases} 1 & ; \quad F(i,j) \geq GTH \\ 0 & ; \quad F(i,j) < GTH \end{cases} \quad (12)$$

effect of applying Equations 11 and 12 to the original digital picture is an outline or edge drawing of objects or areas of constant grey level found in the picture.

2. 3 x 3 Edge Detector

The estimation of the gradient magnitude at a particular pixel can be extended to include the effects of the eight nearest pixels surrounding the pixel of interest. Figure 5 illustrates a 3 x 3 pixel area used to

	y →		
↓	(i-1,j-1)	(i-1,j)	(i-1,j+1)
x	(i,j-1)	(i,j)	(i,j+1)
	(i+1,j-1)	(i+1,j)	(i+1,j+1)
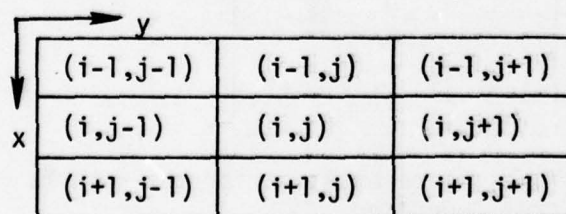
Figure 5. Pixel representation for the 3 x 3
edge operator.

estimate the gradient magnitude at pixel (i,j). The operation of calculating

the gradient magnitude can be defined using an inner or dot product

formulation. Assume that the digital picture function is given by

G(x,y) and an appropriate weighting function by W(x,y), where W is

a 3 x 3 matrix. Then the dot product of G(x,y) with W(x,y) is given by

Equation 13.

$$(G, W)_{i,j} = \sum_{K=1}^{3} \sum_{L=1}^{3} G(i+K-2, j+L-2) W(K,L) \qquad (13)$$

A number of weighting matrices can be found in the literature [2].

Figure 6 illustrates three sets of weighting matrices. The magnitude

$$W_1 \qquad\qquad\qquad W_2$$

$$\begin{bmatrix} 1 & 1 & 1 \\ 0 & 0 & 0 \\ -1 & -1 & -1 \end{bmatrix} \qquad \begin{bmatrix} 1 & 0 & -1 \\ 1 & 0 & -1 \\ 1 & 0 & -1 \end{bmatrix}$$

a. Smoothed gradient

$$\begin{bmatrix} 1 & 2 & 1 \\ 0 & 0 & 0 \\ -1 & -2 & -1 \end{bmatrix} \qquad \begin{bmatrix} 1 & 0 & -1 \\ 2 & 0 & -2 \\ 1 & 0 & -1 \end{bmatrix}$$

b. Sobel weighting functions

$$\begin{bmatrix} 1 & \sqrt{2} & 1 \\ 0 & 0 & 0 \\ 1 & -\sqrt{2} & 1 \end{bmatrix} \qquad \begin{bmatrix} 1 & 0 & -1 \\ \sqrt{2} & 0 & -\sqrt{2} \\ 1 & 0 & -1 \end{bmatrix}$$

c. Isotropic weighting functions

Figure 6. Weighting matrices used for gradient estimation.

of the gradient at pixel(i,j) can be estimated as follows.

Let

$$S_x(i,j) = (G, W_1) \qquad \text{and}$$
$$S_y(i,j) - (G, W_2)$$

(14)

Then the gradient magnitude is given by Equation 15

$$||\nabla g(i,j)|| \simeq [S_x^2(i,j) + S_y^2(i,j)]^{1/2}$$

(15)

A more computationally efficient algorithm is given in Equation 16 and the

quantization process would proceed as given in Equation (12). The most

$$F(i,j) = |S_x(i,j)| + |S_y(i,j)|$$

(16)

common of the three weighting matrices is that due to Sobel and was

chosen as the 3 x 3 edge detector for studies made in this report.

As can be seen from Figures 4 and 5 the binary image arrays are

somewhat reduced in size compared to the original input image array.

If the original image is of size N x M, then the 2 x 2 edge operator

produces a binary array of dimension (N - 1) x (M - 1) and the 3 x 3

edge operator produces a binary image of dimension (N - 2) x (M - 2).

In general if the edge detection operation is based on n x m pixels, the

resulting binary array will be of dimension (N - n + 1) x (M - m + 1).

These reductions of array size present no problems in the correlation

system.

3. Other Edge Detectors

     There are many other types of edge detection algorithms found in

the literature. In most cases they are extensions of the 3 x 3 edge

detector to include the properties of gradient direction and edge point

connectivity. These edge detection schemes were not implemented in the

correlation system study since they would impose more stringent storage

and computation time requirements on the system. However, a brief outline

of how these systems operate will now be given. Figure 7 shows in block

diagram form a more elaborate edge detection system [3]. In this system

the decision to form the binary image is no longer conditioned on threshold

only, but on a combination of gradient activity, threshold, and connectivity

of the edge direction to other pixels. The gradient picture is formed by
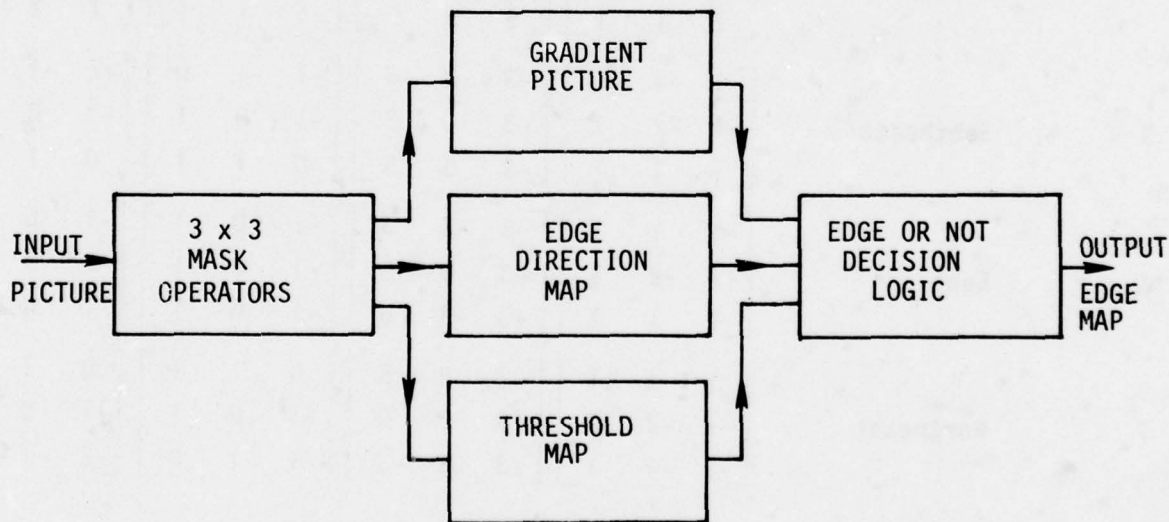
Figure 7. A more elaborate edge detection system.

selecting the maximum magnitude produced by any one of the sets of masks

shown in Figure 8. The direction of the gradient is chosen by which

mask produces the maximum magnitude output. Figure 9 illustrates the

Direction of Edge	Direction of Gradient	Prewitt Masks	Kirsch Masks	Three-level Simple Masks	Five-level Simple Masks
0	North	$\begin{bmatrix} 1 & 1 & 1 \\ 1 & -2 & 1 \\ -1 & -1 & -1 \end{bmatrix}$	$\begin{bmatrix} 5 & 5 & 5 \\ -3 & 0 & -3 \\ -3 & -3 & -3 \end{bmatrix}$	$\begin{bmatrix} 1 & 1 & 1 \\ 0 & 0 & 0 \\ -1 & -1 & -1 \end{bmatrix}$	$\begin{bmatrix} 1 & 2 & 1 \\ 0 & 0 & 0 \\ -1 & -2 & -1 \end{bmatrix}$
1	Northwest	$\begin{bmatrix} 1 & 1 & 1 \\ 1 & -2 & -1 \\ 1 & -1 & -1 \end{bmatrix}$	$\begin{bmatrix} 5 & 5 & -3 \\ 5 & 0 & -3 \\ -3 & -3 & -3 \end{bmatrix}$	$\begin{bmatrix} 1 & 1 & 0 \\ 1 & 0 & -1 \\ 0 & -1 & -1 \end{bmatrix}$	$\begin{bmatrix} 2 & 1 & 0 \\ 1 & 0 & -1 \\ 0 & -1 & -2 \end{bmatrix}$
2	West	$\begin{bmatrix} 1 & 1 & -1 \\ 1 & -2 & -1 \\ 1 & 1 & -1 \end{bmatrix}$	$\begin{bmatrix} 5 & -3 & -3 \\ 5 & 0 & -3 \\ 5 & -3 & -3 \end{bmatrix}$	$\begin{bmatrix} 1 & 0 & -1 \\ 1 & 0 & -1 \\ 1 & 0 & -1 \end{bmatrix}$	$\begin{bmatrix} 1 & 0 & -1 \\ 2 & 0 & -2 \\ 1 & 0 & -1 \end{bmatrix}$
3	Southwest	$\begin{bmatrix} 1 & -1 & -1 \\ 1 & -2 & -1 \\ 1 & 1 & 1 \end{bmatrix}$	$\begin{bmatrix} -3 & -3 & -3 \\ 5 & 0 & -3 \\ 5 & 5 & -3 \end{bmatrix}$	$\begin{bmatrix} 0 & -1 & -1 \\ 1 & 0 & -1 \\ 1 & 1 & 0 \end{bmatrix}$	$\begin{bmatrix} 0 & -1 & -2 \\ 1 & 0 & -1 \\ 2 & 1 & 0 \end{bmatrix}$
4	South	$\begin{bmatrix} -1 & -1 & -1 \\ 1 & -2 & 1 \\ 1 & 1 & 1 \end{bmatrix}$	$\begin{bmatrix} -3 & -3 & -3 \\ -3 & 0 & -3 \\ 5 & 5 & 5 \end{bmatrix}$	$\begin{bmatrix} -1 & -1 & -1 \\ 0 & 0 & 0 \\ 1 & 1 & 1 \end{bmatrix}$	$\begin{bmatrix} -1 & -2 & -1 \\ 0 & 0 & 0 \\ 1 & 2 & 1 \end{bmatrix}$
5	Southeast	$\begin{bmatrix} -1 & -1 & 1 \\ -1 & -2 & 1 \\ 1 & 1 & 1 \end{bmatrix}$	$\begin{bmatrix} -3 & -3 & -3 \\ -3 & 0 & 5 \\ -3 & 5 & 5 \end{bmatrix}$	$\begin{bmatrix} -1 & -1 & 0 \\ -1 & 0 & 1 \\ 0 & 1 & 1 \end{bmatrix}$	$\begin{bmatrix} -2 & -1 & 0 \\ -1 & 0 & 1 \\ 0 & 1 & 2 \end{bmatrix}$
6	East	$\begin{bmatrix} -1 & 1 & 1 \\ -1 & -2 & 1 \\ -1 & 1 & 1 \end{bmatrix}$	$\begin{bmatrix} -3 & -3 & 5 \\ -3 & 0 & 5 \\ -3 & -3 & 5 \end{bmatrix}$	$\begin{bmatrix} -1 & 0 & 1 \\ -1 & 0 & 1 \\ -1 & 0 & 1 \end{bmatrix}$	$\begin{bmatrix} -1 & 0 & 1 \\ -2 & 0 & 2 \\ -1 & 0 & 1 \end{bmatrix}$
7	Northeast	$\begin{bmatrix} 1 & 1 & 1 \\ -1 & -2 & 1 \\ -1 & -1 & 1 \end{bmatrix}$	$\begin{bmatrix} -3 & 5 & 5 \\ -3 & 0 & 5 \\ -3 & -3 & -3 \end{bmatrix}$	$\begin{bmatrix} 0 & 1 & 1 \\ -1 & 0 & 1 \\ -1 & -1 & 0 \end{bmatrix}$	$\begin{bmatrix} 0 & 1 & 2 \\ -1 & 0 & 1 \\ -2 & -1 & 0 \end{bmatrix}$

Figure 8. Directional weighting matrices.

principal directions selected. It should be noted from Figure 8 that
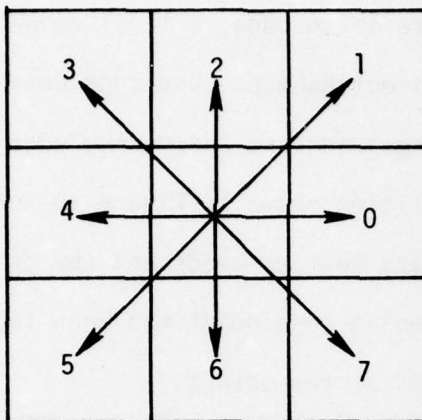
Figure 9. Principle directions of edges.

in the case of the three-level and five-level simple masks only the gradient value of the first four masks need be calculated. The direction of the edge is then given by the sign of the gradient value of the mask producing the maximum absolute gradient value. The edge directions at each pixel generate the edge direction map shown in Figure 7. The threshold map shown in Figure 7 is normally produced by a locally adaptive process such as the one given in [3]. This method is given in Equation 17, where LAT is the locally adaptive threshold.

$$LAT = \frac{MAX\ \{|Y_k|\ ,\ k = 0,1,\ldots,7\}}{Output\ of\ the\ low\ pass\ filter\ M_o\ at\ pixel\ (i,j)} \quad (17)$$

where Y_k, $k = 0,1,\ldots,7$ are the gradient values at pixel (i,j) and

$$M_o = \frac{1}{16} \begin{bmatrix} 1 & 2 & 1 \\ 2 & 4 & 2 \\ 1 & 2 & 1 \end{bmatrix}$$

The process of Equation 17 is one of comparing the gradient image with a

blurred version of the original image produced by the low-pass operation in the denominator.

In determining if there is an edge, a local connectivity test is performed using the edge direction map. One such connectivity test is shown in Figure 10. The preceding and succeeding edge directions must satisfy one of the possibilities shown in Figure 10 for the test to succeed. If the connectivity test succeeds and the gradient value is above the threshold, then an edge point has been found. Thus, the binary edge map is generated at the output.
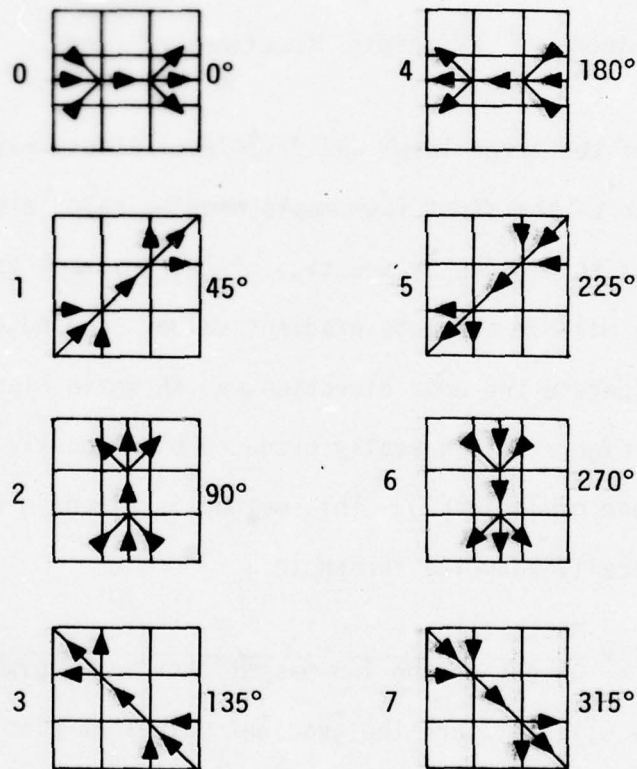
Figure 10. Local connectivity test of edge directions.

3. SIMULATION RESULTS OF THE
CORRELATION SYSTEM

This chapter describes the simulation program, developed by contract personnel, used to study the effects of the preprocessors described in Chapter 2. Section A provides a general explanation and block diagram of the simulation program. A complete listing and detailed flow charts of the simulation program are compiled as a supplement to this report and can be obtained from the project director. This chapter also presents explanations and results of studies conducted using the correlation system simulation program.

A. The Simulation Program

In order to analyze the effects on the correlation system of the various preprocessors given in Chapter 2, it was necessary that a generalized correlation system simulation program be written. Figure 11 illustrates a *correlator hand-off system* as proposed in [4]. The simulation program is structured to perform all functions illustrated by Figure 11 through the calculation of the correlation array. Figure 12 shows in block diagram form the functions performed by the simulation program. The simulation program is coded using the FORTRAN language and structured in subroutine format for ease in substitution or modification of algorithms.

A general description of the operation of the program will now be given.
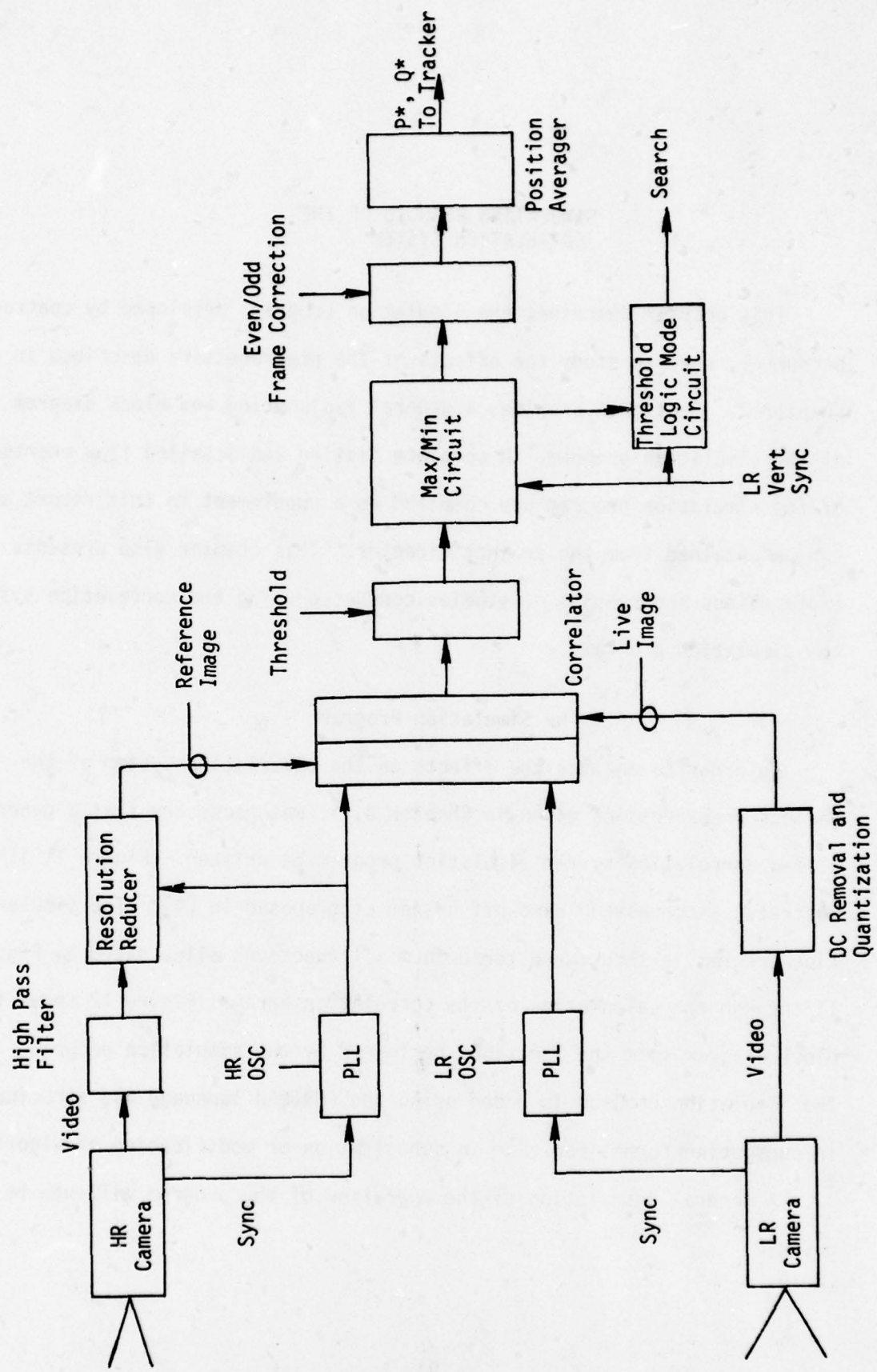
Figure 11. Block diagram of correlator hand-off system.
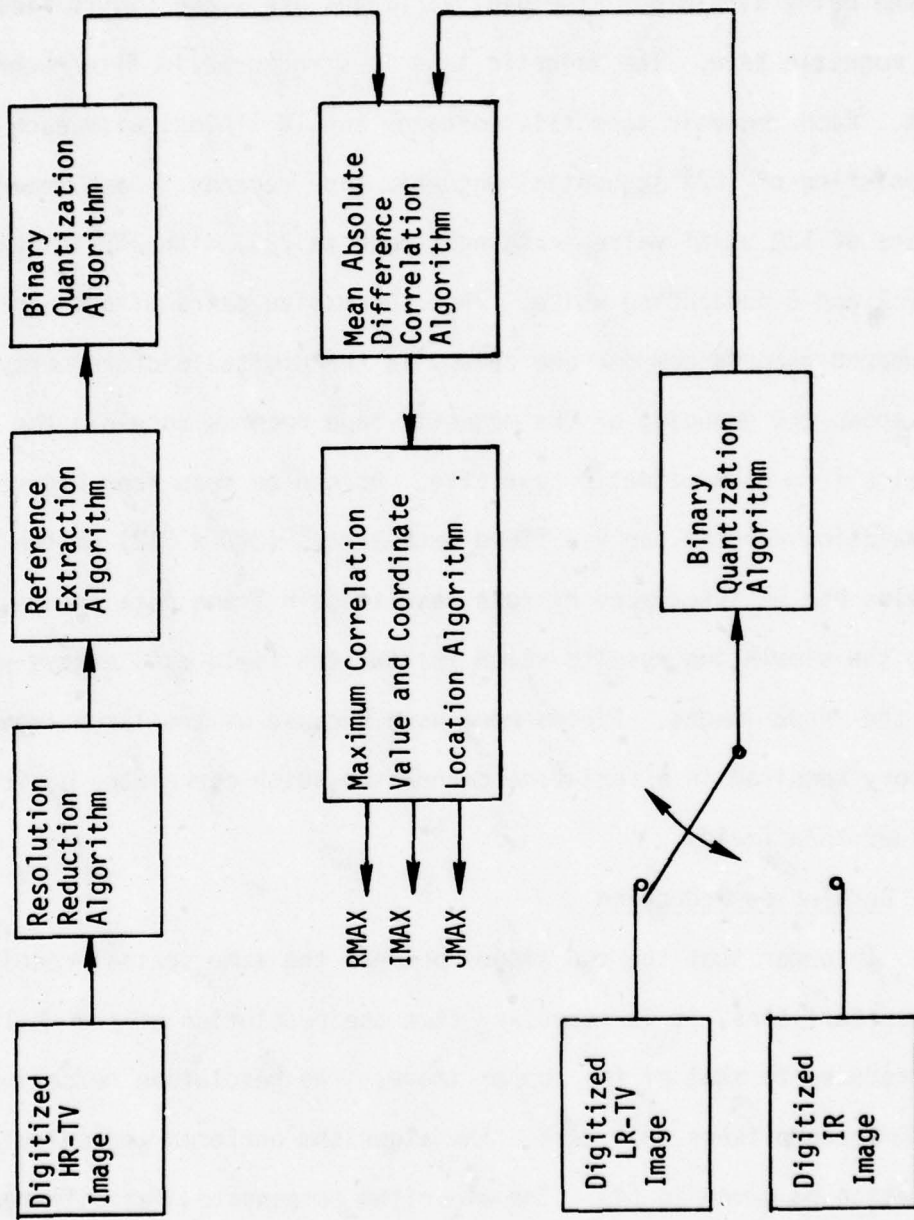
Figure 12. Block diagram of correlation system simulation program.

1. Image Input

The simulation program receives as input digitized images of the scene being simulated. The digital images are stored in TV field arrays on magnetic tape. The magnetic tape is structured in file/record format. Each magnetic tape file contains two TV fields, with each field consisting of 1024 sequential magnetic tape records. Each record consists of 120 pixel values ranging from 0 to 225, with 255 indicating black and 0 indicating white. Thus successive pairs of odd and even numbered records compose one column in the digital picture array. Figure 13 shows the grouping of the magnetic tape records to yield the two TV fields from each magnetic tape file. As can be seen from Figure 13 the simulation program can use field data arrays (240 x 512) or the two fields can be interlaced by rows resulting in frame data arrays (480 x 512). For the simulation results which follow, the field data arrays were used as the input images. Fields were used because of the large amount of memory required in a real-time correlator which correlates on frames rather than fields.

2. Resolution Reduction

In order that the two images possess the same spatial resolution characteristics, it is necessary that the resolution of the HR-TV image be reduced to that of the sensor image. The resolution reduction algorithm accomplishes this task. The algorithm performs the calculations of Equation 67 given in [4]. The algorithm compensates for differences in resolution between the HR-TV image and the sensor image caused by differing fields of view, number of TV lines per frame, frame rate, aspect ratio,
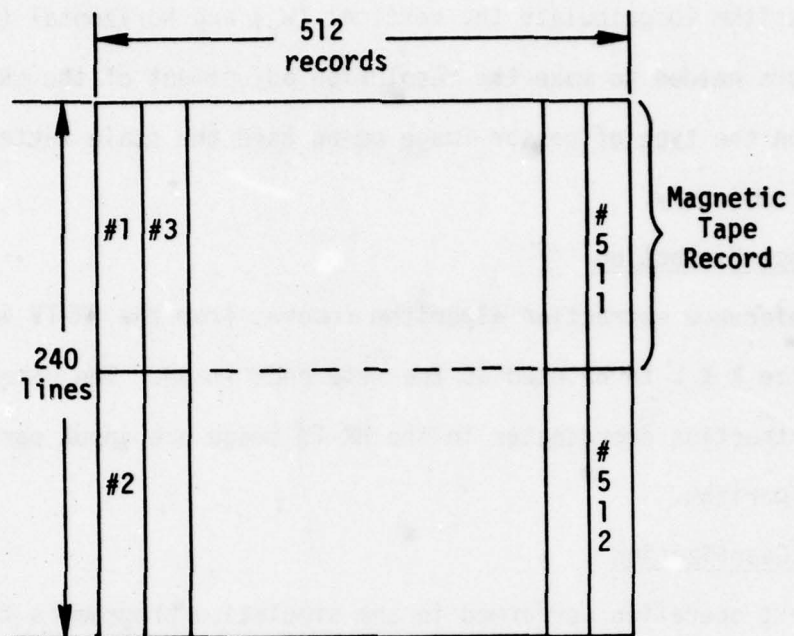
a. Field 1.
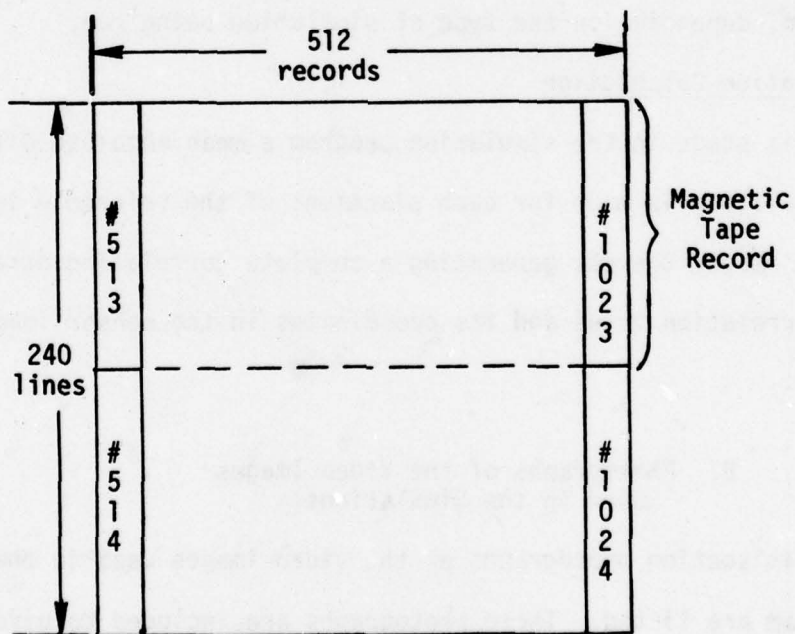
b. Field 2.

Figure 13. Layout of a magnetic tape file of a
digital picture.

and sampling rate of the two imaging systems. These parameters are used by the algorithm to calculate the vertical (W_V) and horizontal (W_H) scale factors needed to make the resolution adjustment of the HR-TV image. Depending on the type of sensor image being used the scale factors would change appropriately.

3. Reference Extraction

The reference extraction algorithm removes from the HR-TV image an array of size K X L to be used as the reference image. The reference size and extraction coordinates in the HR-TV image are input parameters for this algorithm.

4. Binary Quantization

The next operation performed in the simulation program is that of binary quantization. One of the preprocessors of Chapter 2 would be implemented, depending on the type of simulation being run.

5. Correlation Calculation

At this stage in the simulation program a mean absolute difference (MAD) calculation is made for each placement of the reference image in the sensor image, thereby generating a complete correlation array. The maximum correlation value and its coordinates in the sensor image are identified.

B. Photographs of the Video Images Used in the Simulations

In this section photographs of the video images used in the simulation program are listed. These photographs are included to give the reader some idea as to what types of scenes were tested. The simulation

results given in the next section will refer to the scenes as they are

numbered in this list. The abbreviations used in the titles on the

photographs are as follows:

NFOV - Narrow field of view
WFOV - Wide field of view
IRIS - Infra-Red Imaging Seeker
WH - White Hot
TV - Television

Also included in this section are computer generated density and edge

plots of Scene 6. Figure 29(a) is a computer generated image of Scene 6

NFOV-TV with a vertical and horizontal scale factor of 4 where the grey

scale data has been reduced to 10 shades. Figures 29(b) through 29(g)

are plots of the 2 x 2 and 3 x 3 edge detection algorithms using three

threshold levels for edge discrimination. Figure 30 and 31 are the binary

images produced by the 2 x 2 and 3 x 3 edge detection algorithms using the

HR-TV and IRIS-WH images. The HR-TV horizontal and vertical scale factors

used were 4.722 x 18.0, respectively. The edge plots are shown for three

different gradient threshold settings to give the reader an idea of the

difference produced by the two edge detection algorithms.

C. Results of the Average Value Preprocessors

In this section the results of simulations carried out using the

average value preprocessors are presented. While the main thrust of this

contract was to find a correlation system configuration to handle TV to IR

Correlations, TV-to-TV simulations were attempted to support to results

given in [4]. Table 1 illustrates the simulation results of TV-to-TV

correlations for scenes 1 to 4. As given in Table 1 the correlations

were implemented by extracting the reference array from the High Resolution
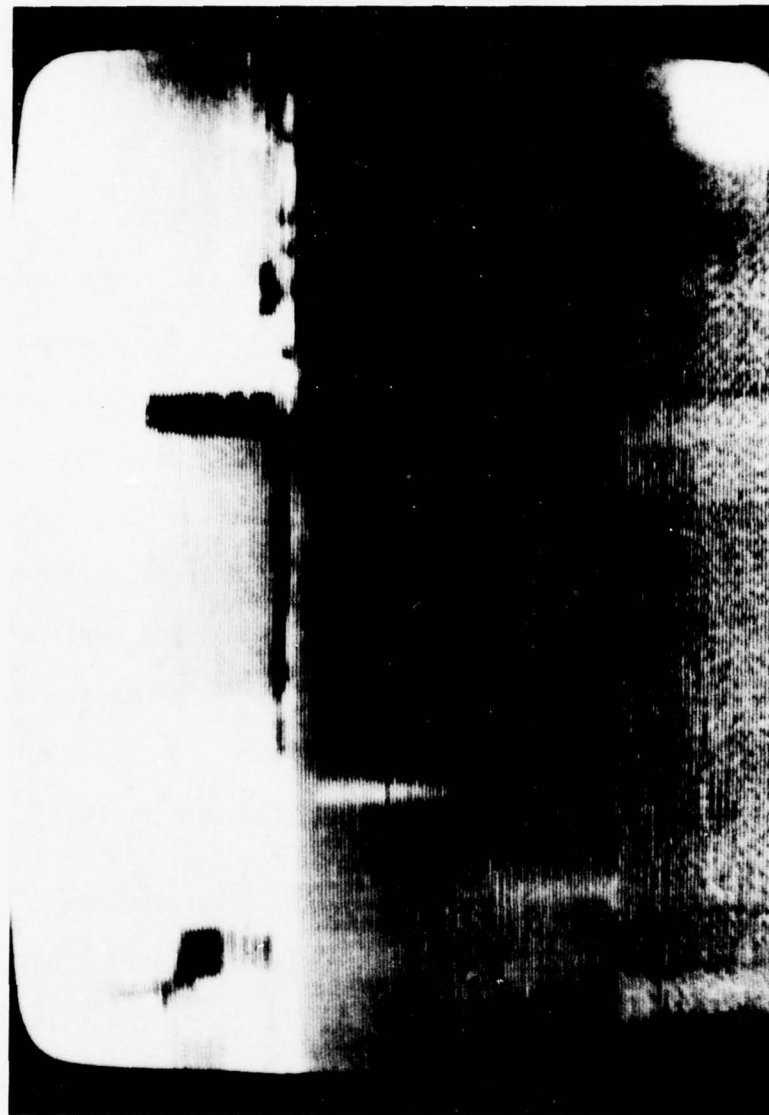
Figure 14. Scene 1 NFOV - TV - NASA tower.

Figure 15. Scene 1 WFOV - TV - NASA tower.
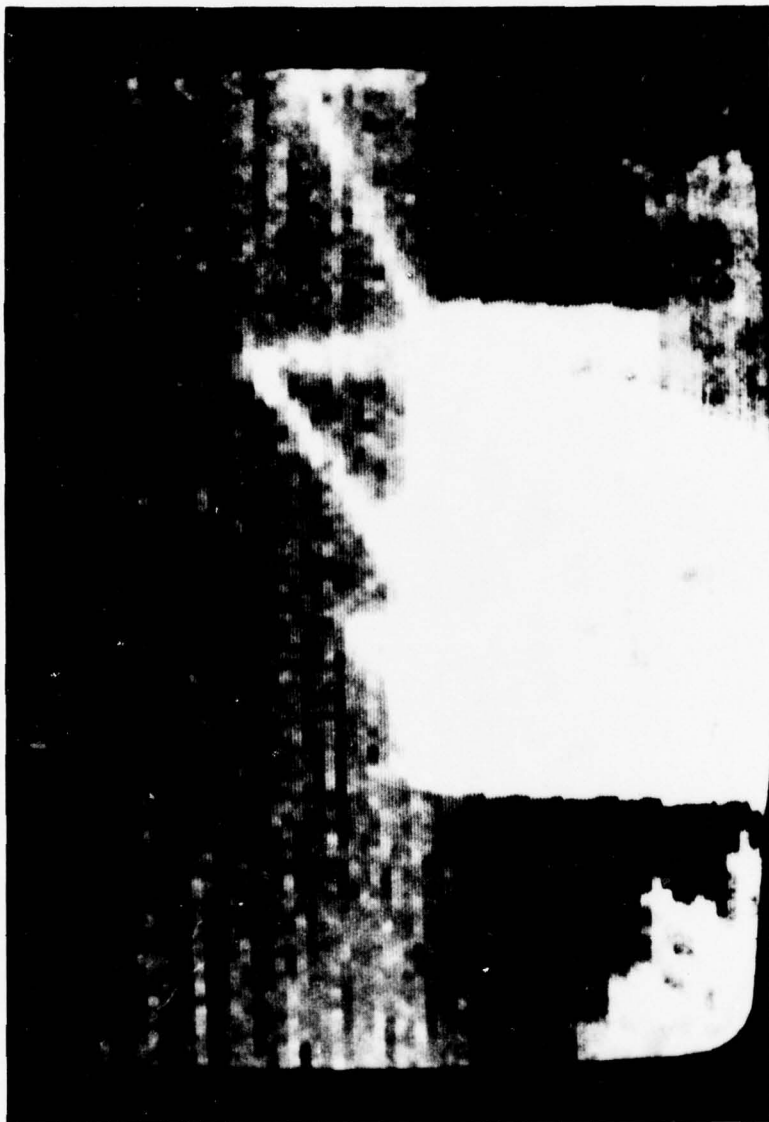
Figure 16.   Scene 1   IRIS - WH - NASA tower.

35

Figure 17.   Scene 2   NFOV - TV - Water tank.

Figure 18. Scene 2 IRIS - WH - Water tank.

Figure 19. Scene 3 NFOV - TV - Woods.

Figure 20. Scene 3 IRIS - WH - Woods.

Figure 21.   Scene 4   NFOV - TV - Parking Lot
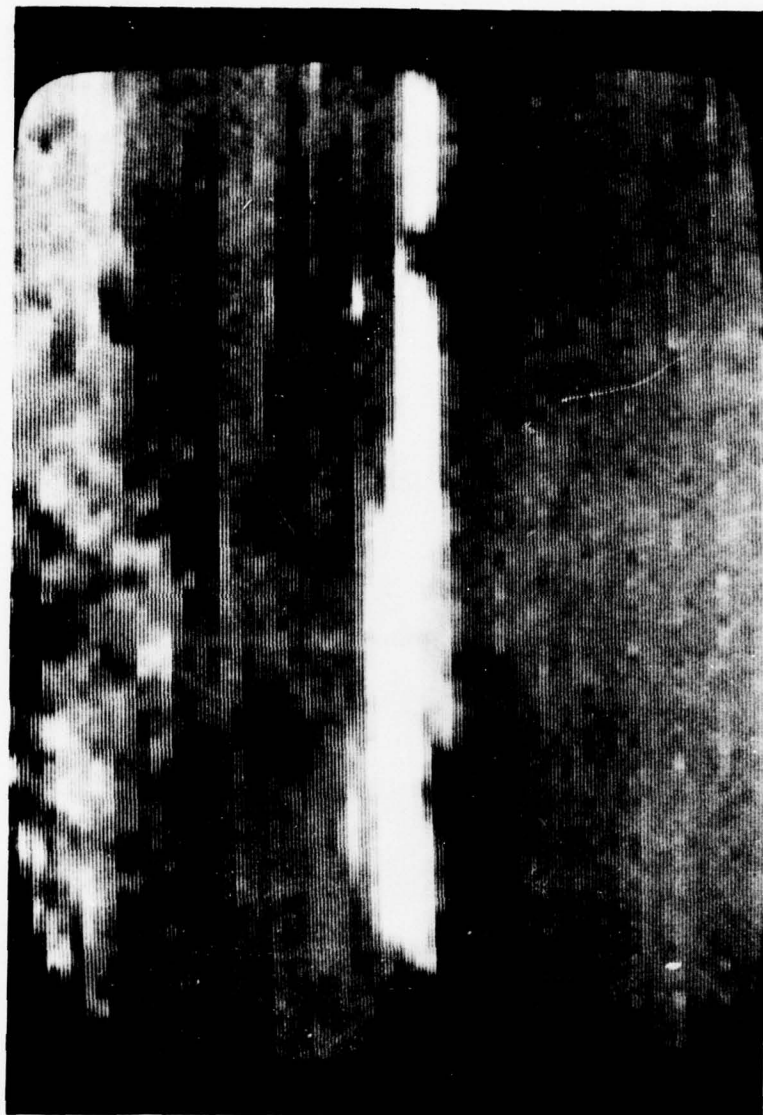
Figure 22. Scene 4 IRIS – WH – Parking lot.

Figure 23. Scene 5 NFOV - TV - Jeep in Parking lot.

Figure 24. Scene 5 IRIS - WH - Jeep in Parking Lot.

Figure 25. Scene 6 NFOV - TV - Jeep in front of fence.

Figure 26. Scene 6 IRIS - WH - Jeep in front of fence.

Figure 27. Scene 7 NFOV - TV - Jeep behind fence.

Figure 28. Scene 7 IRIS - WH - Jeep behind fence.
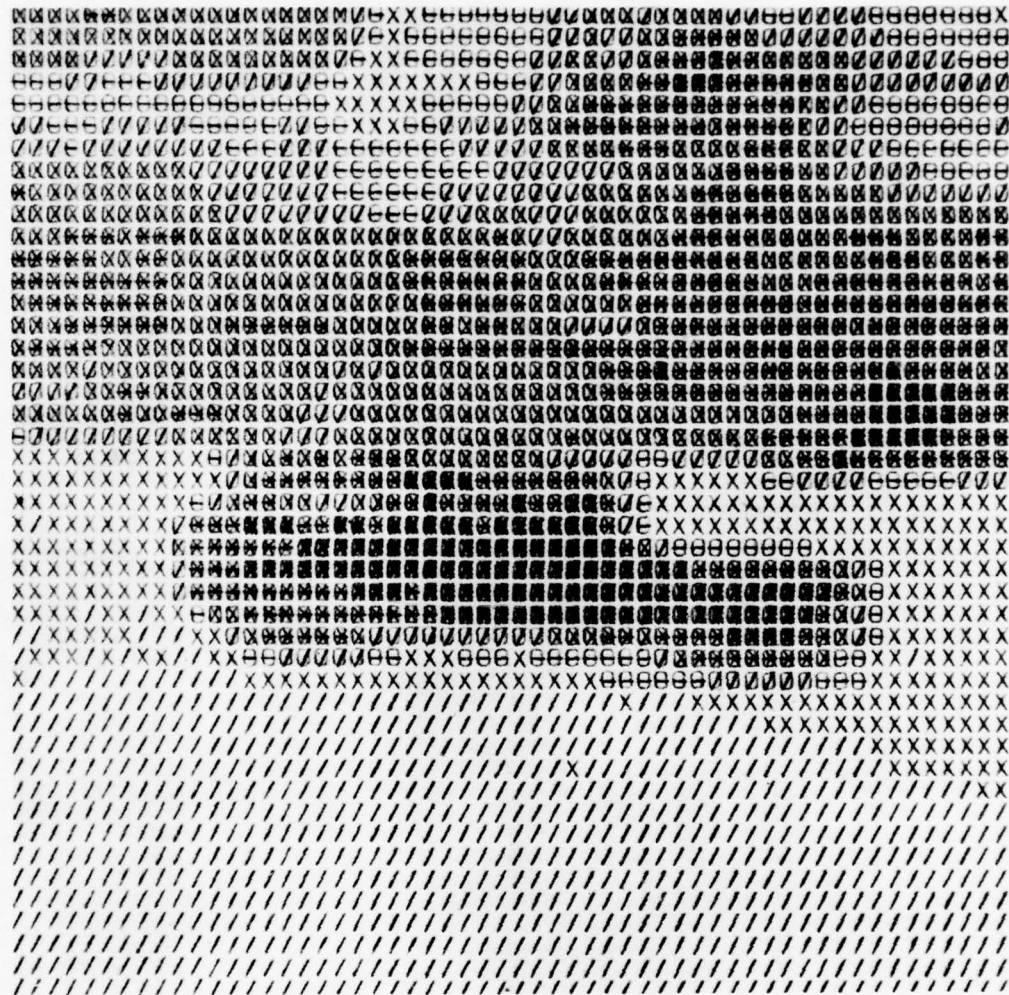
a. Ten-level density plot.

Figure 29. Computer generated images for Scene 6-NFOV-TV with W_H=4.0 and W_V=4.0

Figure 29b. Output of 2 x 2 edge detector with gradient threshold=10.0
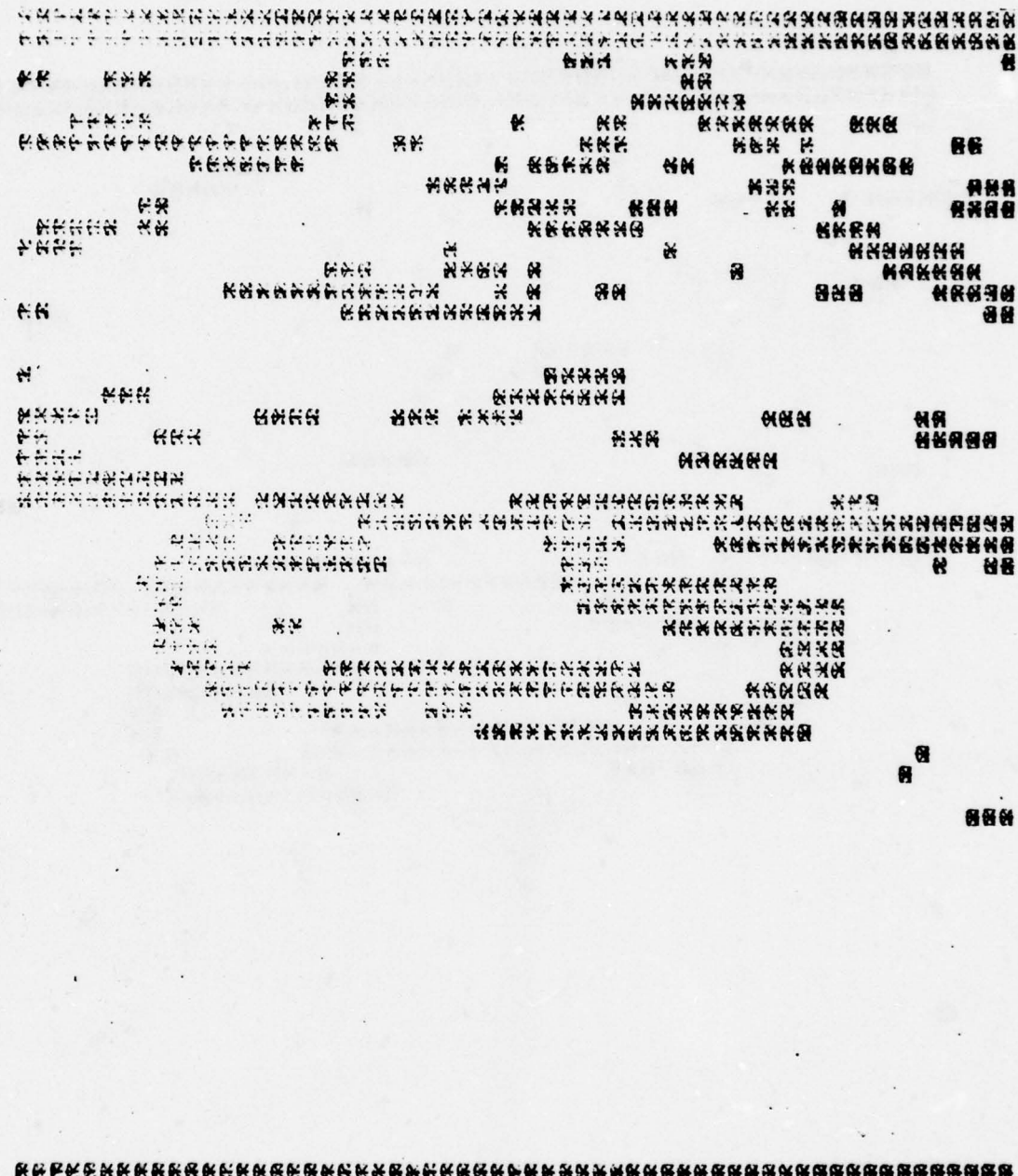
Figure 29c. Output of 2 x 2 edge detector with gradient threshold=30.0
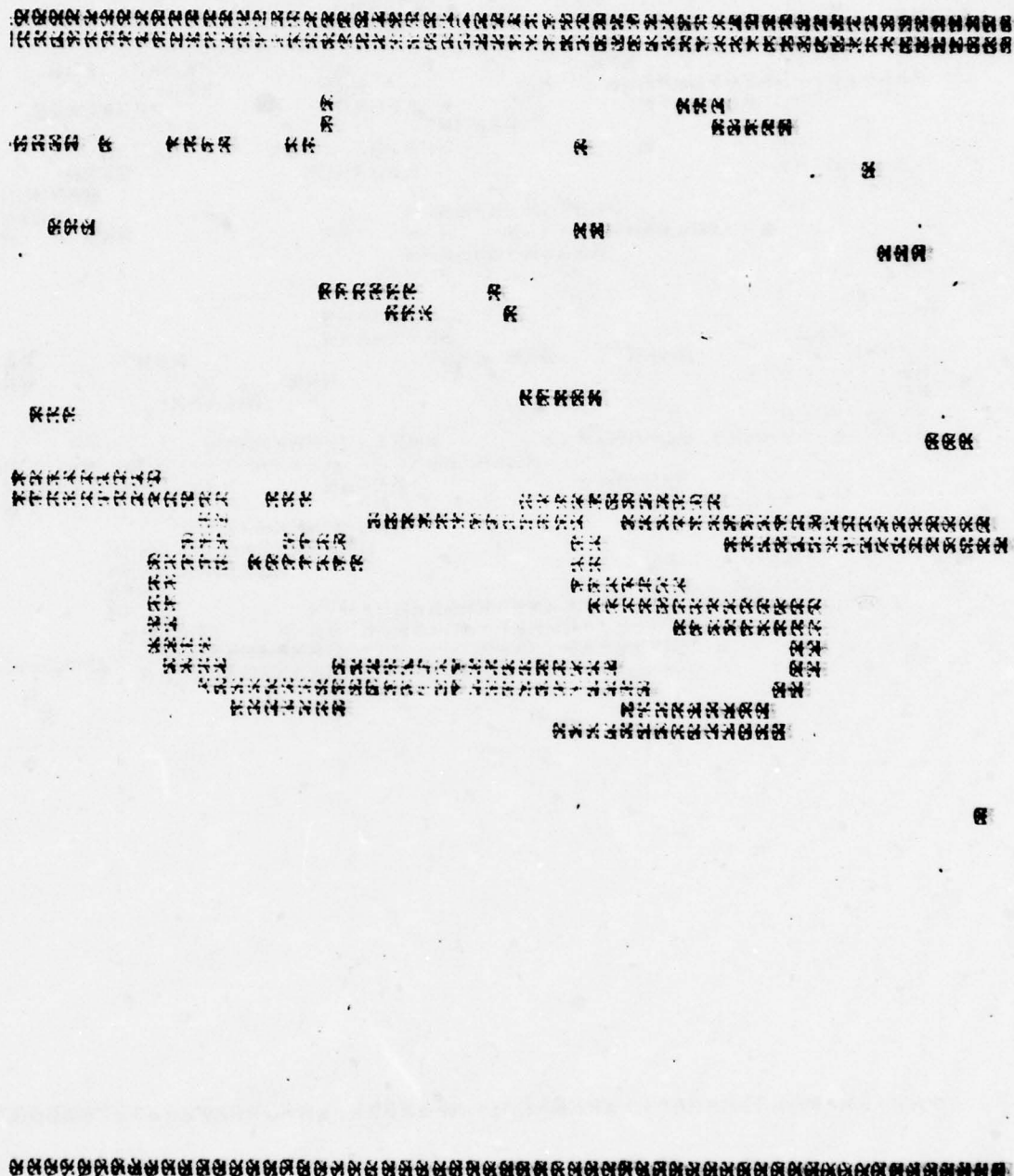
Figure 29d. Output of 2 x 2 edge detector with gradient threshold=50.0

Figure 29e. Output of 3 x 3 edge detector with gradient threshold=50.0

Figure 29f. Output of 3 x 3 edge detector with gradient threshold=100.0

Figure 29g. Output of 3 x 3 edge detector with gradient threshold=150.0

54
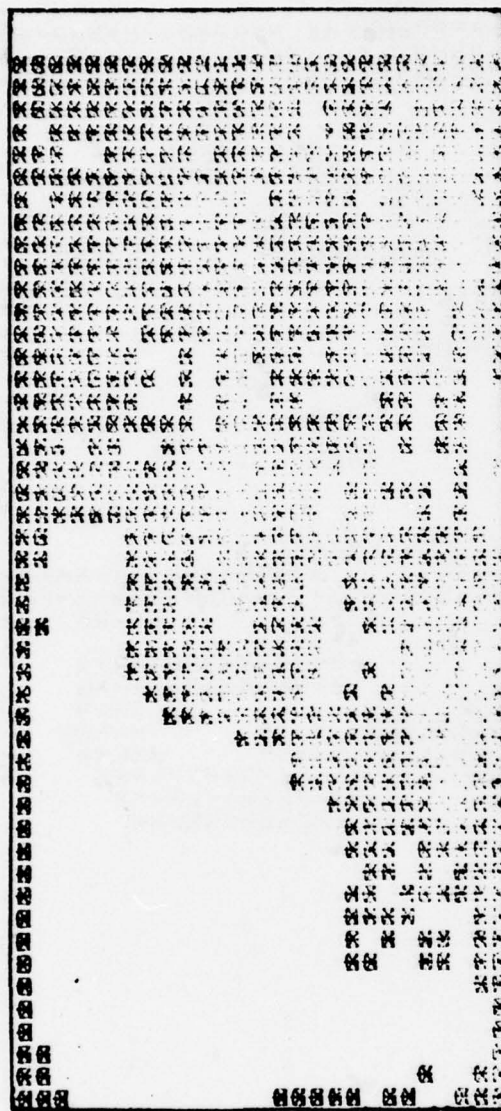
Figure 30a. NFOV-TV
            GTH=10.0

Figure 30b. IRIS
            GTH=20.0

* GTH=Gradient Threshold

Figure 30. Output of 2 x 2 edge detector for Scene 6 with W_H=18.0 and W_V=4.722

Figure 30c. NFOV-TV
GTH=30.0
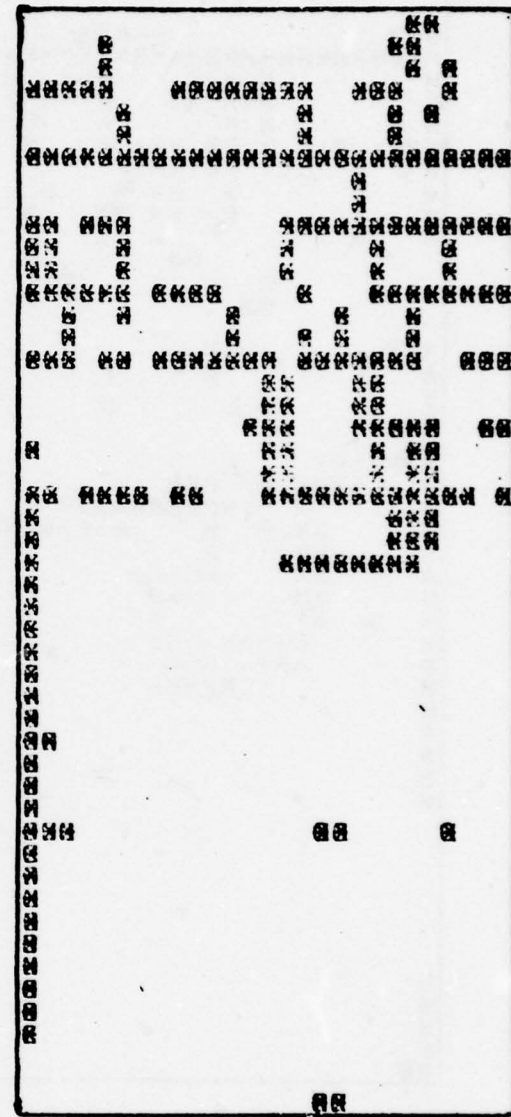
Figure 30d. IRIS
GTH=40.0

56
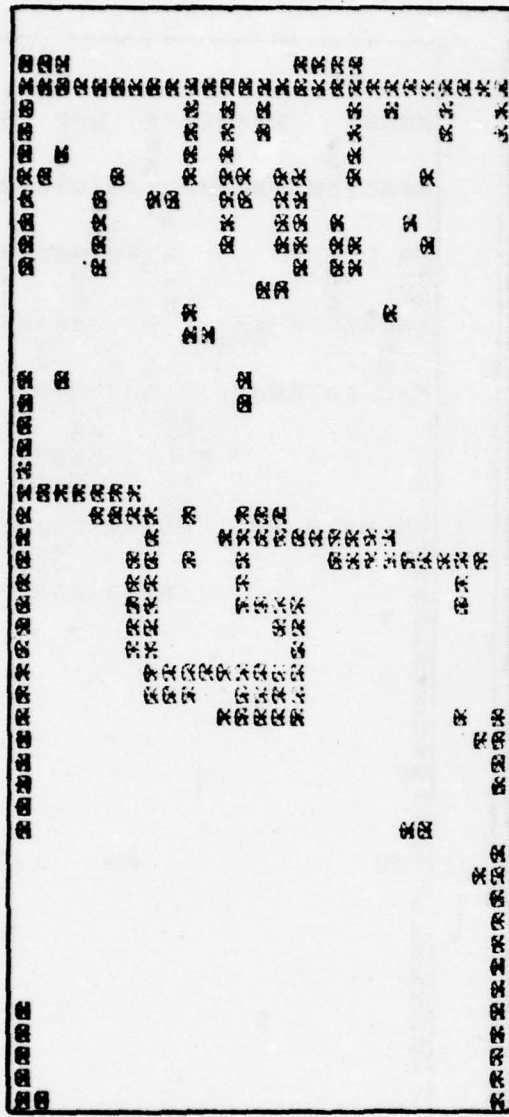
Figure 30e. NFOV-TV
            GTH=50.00
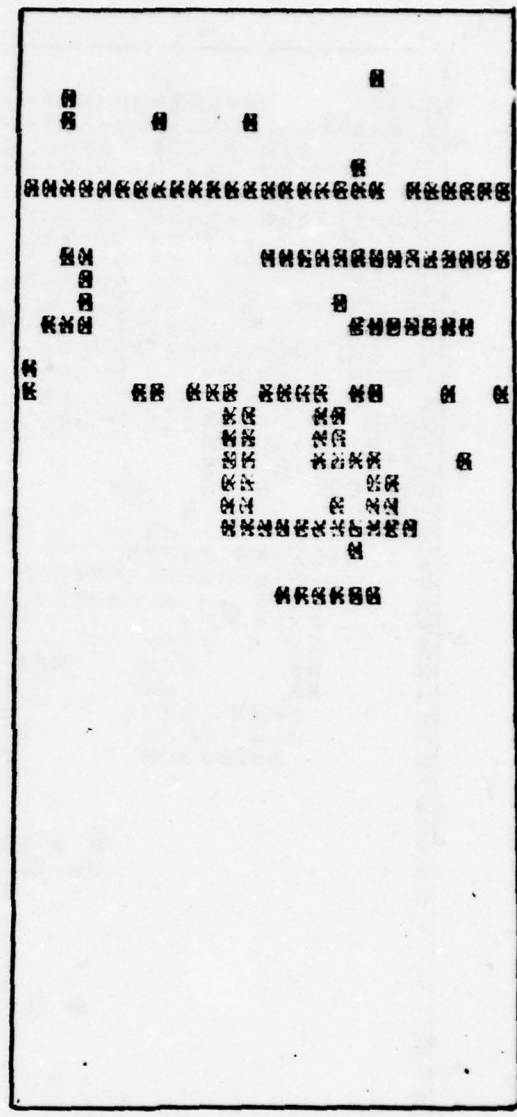
Figure 30f. IRIS
            GTH=60.0
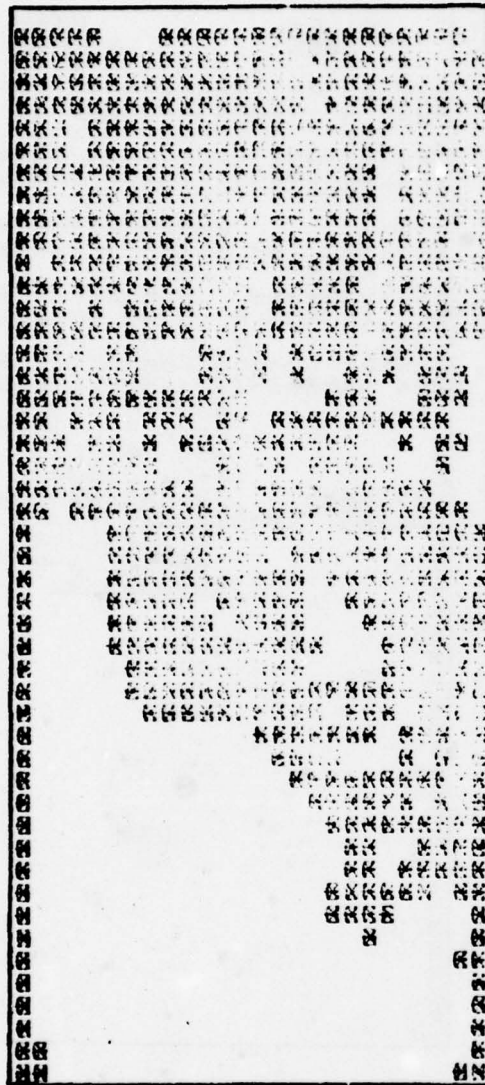
Figure 31a. NFOV-TV
            GTH=50.0
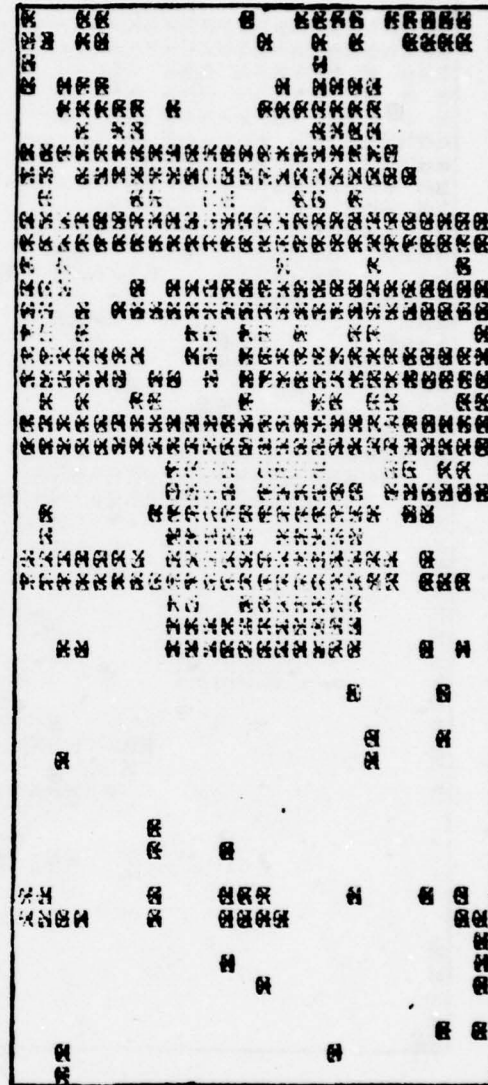
Figure 31b. IRIS
            GTH=80.0

Figure 31. Output of 3 x 3 edge detector for Scene 6 with W_H=18.0
           and W_V=4.722

58
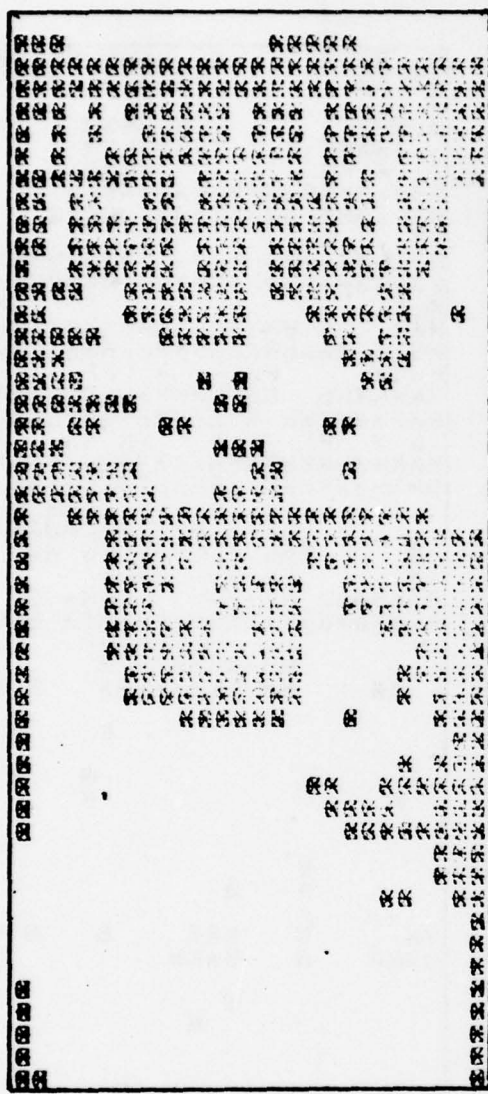
Figure 31c. NFOV-TV
           GTH=100.0
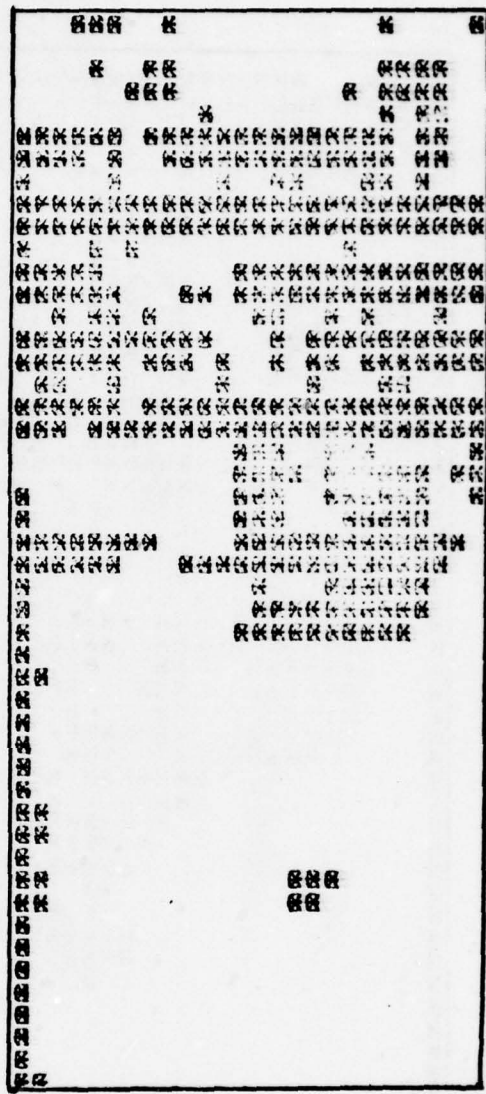
Figure 31d. IRIS
           GTH=100.0
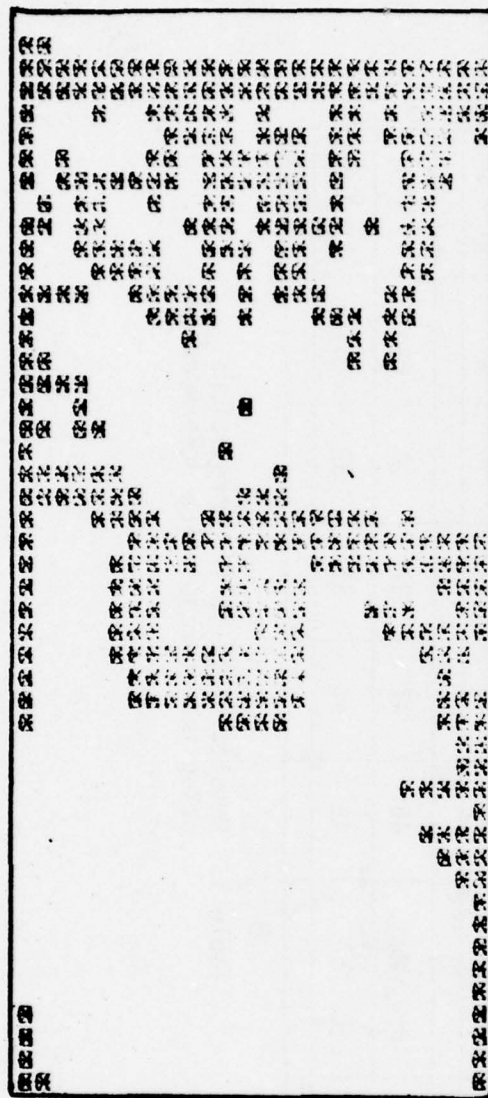
Figure 31e. NFOV-TV
         GTH=150.0
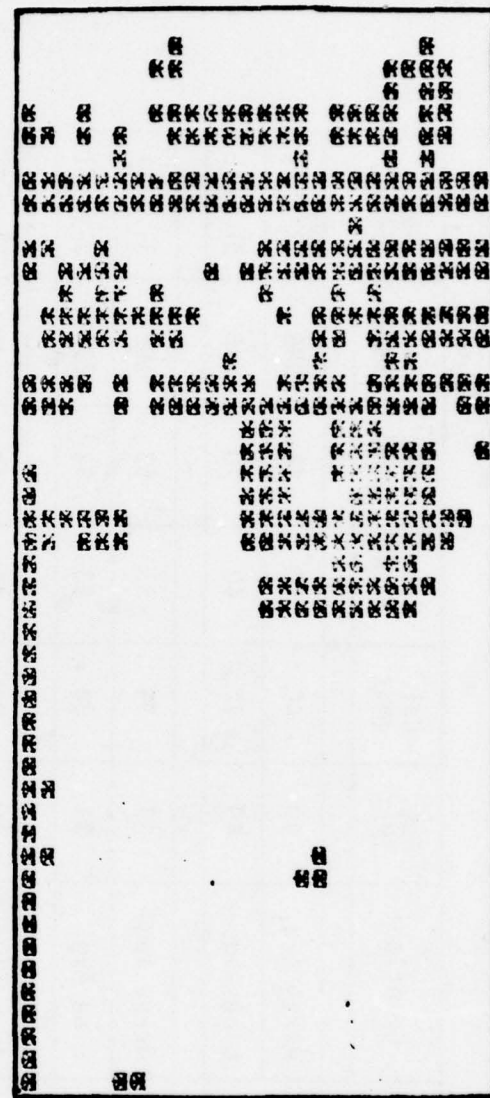
Figure 31f. IRIS
         GTH=120.0

Scene	Quantizer	Est. IMAX	Cal. IMAX	Est. JMAX	Cal. JMAX	Cal. RMAX	Ref. Size
1	Array Avg.	40	40	40	41	598	31 x 31
	Line Avg.	40	42	40	40	646	31 x 31
2	Array Avg.	39	39	53	53	602	31 x 31
	Line Avg.	39	38	53	54	620	31 x 31
3	Array Avg.	39	39	47	44	634	31 x 31
	Line Avg.	39	39	47	48	607	31 x 31
4	Array Avg.	46	47	37	38	694	31 x 31
	Line Avg.	46	43	37	35	613	31 x 31

Table 1. Results of TV-to-TV correlations using the average value preprocessors.

(HR) - TV image. This reference was then matched to that of the Low-Resolution (LR) - TV image. The estimated match coordinates in the LR image, given by Est. IMAX and Est. JMAX in the table, were found by visually inspecting density plots of the images under test. The values Cal. IMAX and Cal. JMAX were found using the computer simulation. The value Cal. RMAX is the maximum correlation value computed. In all cases given in Table 1 the reference size was chosen to be 31 x 31 yielding a possible maximum correlation value of 961. The line average sample length was set at 11 and the array average sample size was set at 11 x 11.

As can be seen from Table 1 the estimated and calculated match coordinates are very close with a difference of only a few pixels in most simulations. This indicates that the line average and array average preprocessors work well for TV-to-TV correlations carried out on images with a wide variety of spectral characteristics. Cross-sectional plots of the correlation function generated through the maximum value along the I and J axis also give some insight into the "goodness" of the preprocessors. Figures 32 through 35 show the cross-sectional plots from simulations made on scenes 1 and 4 in Table 1. These plots show that the line average quantizer produces a sharper correlation peak than does the array average quantizer. The more well defined correlation peak was also evident in the cross-sectional plots of the other simulations using the line average quantizer listed in Table 1.

The next set of simulations tried were those in which the sensor image was acquired using the IRIS and the average value preprocessors were used for binary conversion. The results of these simulations are
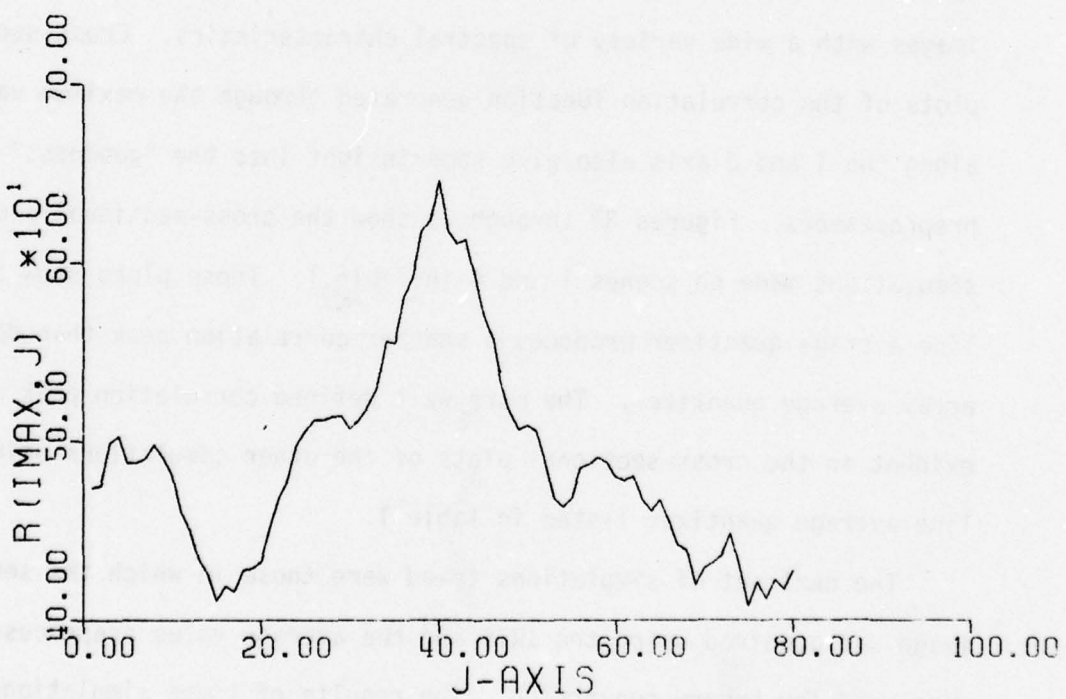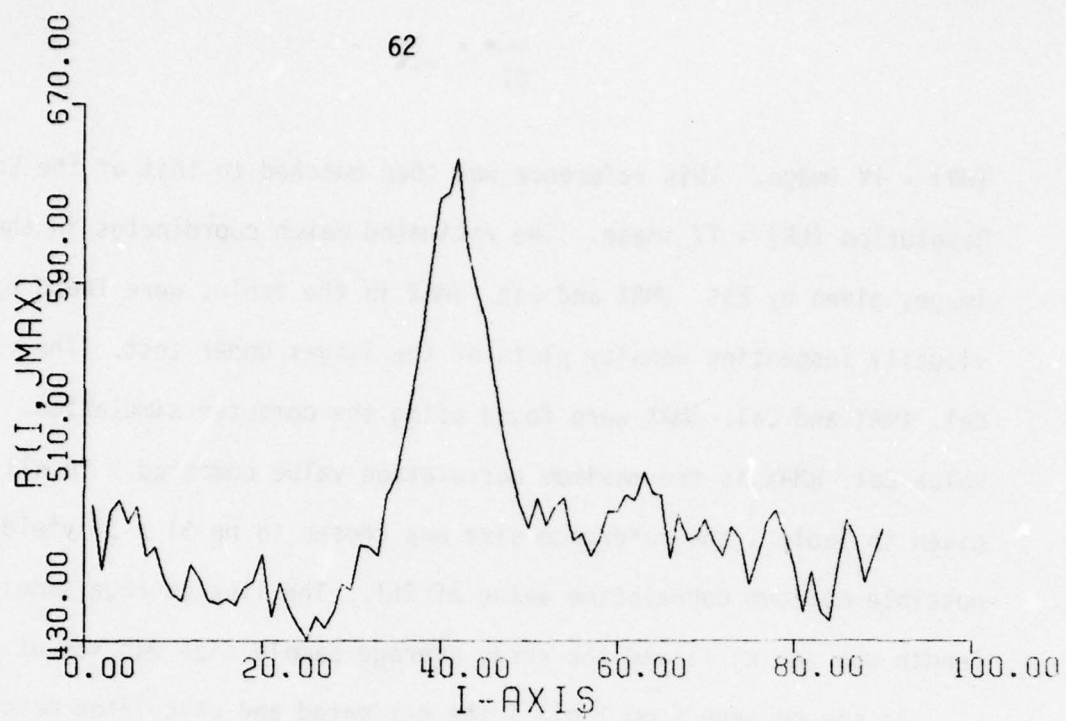
Figure 32. Cross-sectional plots of scene 1 correlation
using the line average quantizer.
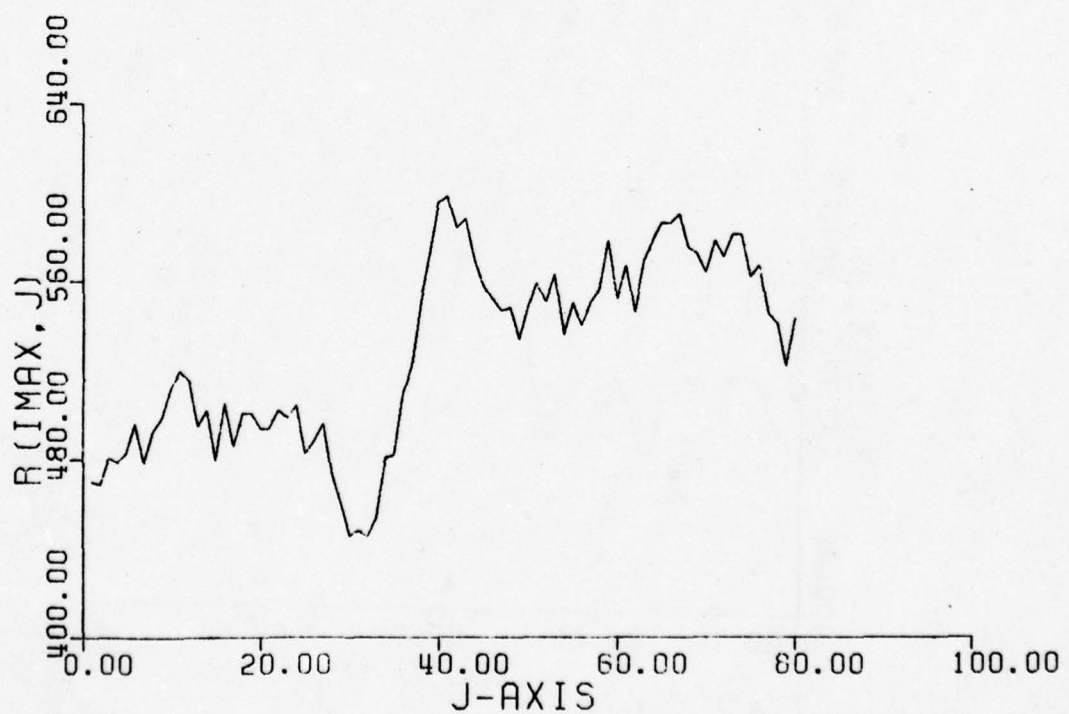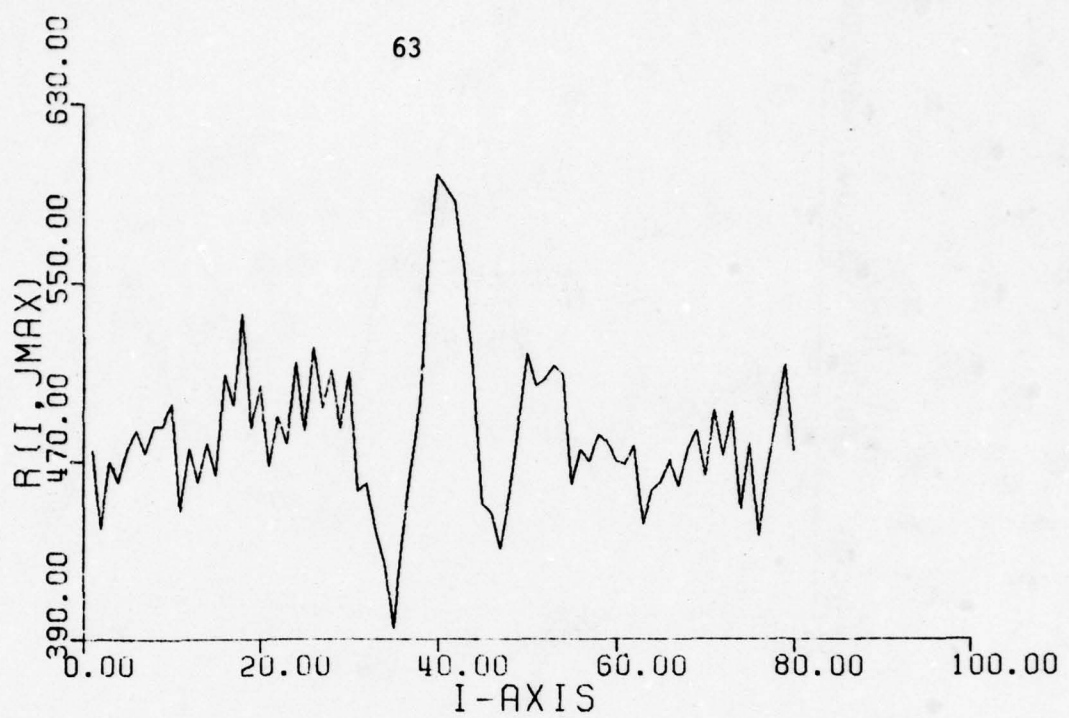
Figure 33. Cross-sectional plots of scene 1 correlation using the array average quantizer.
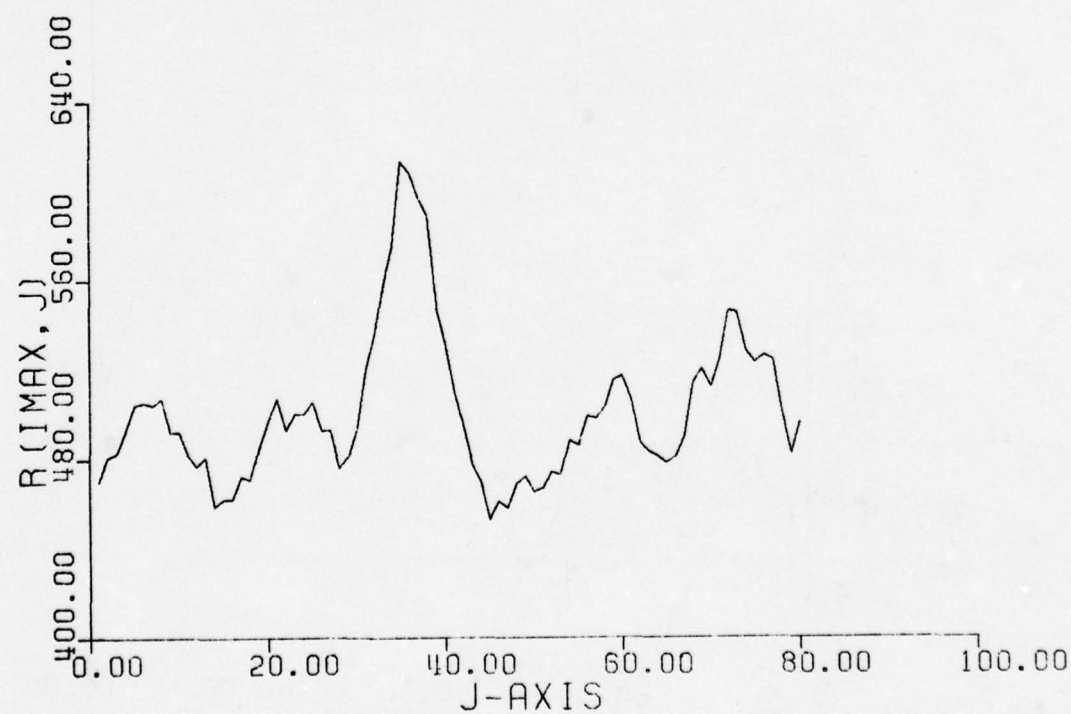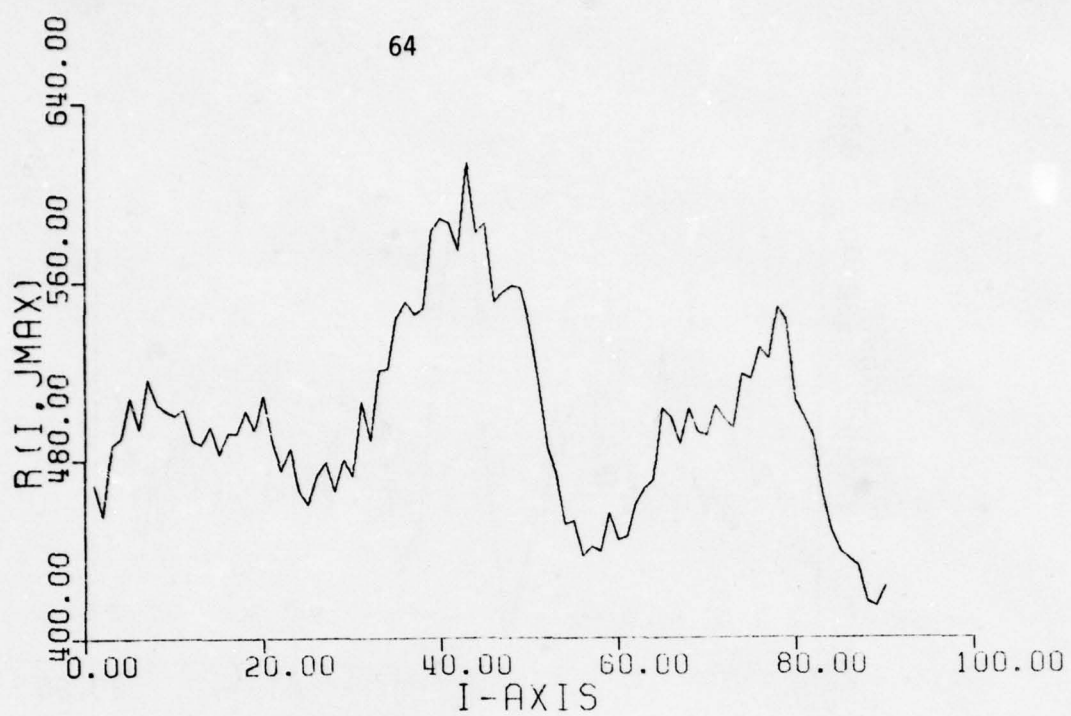
Figure 34. Cross-sectional plots of scene 4 correlation
using the line average quantizer.
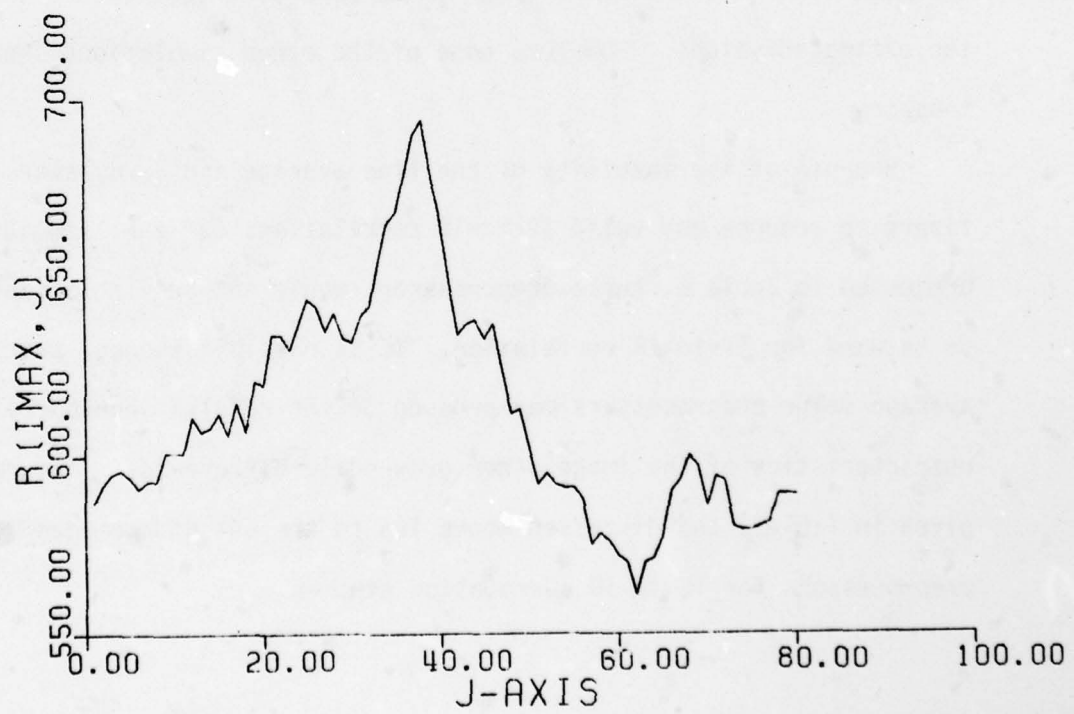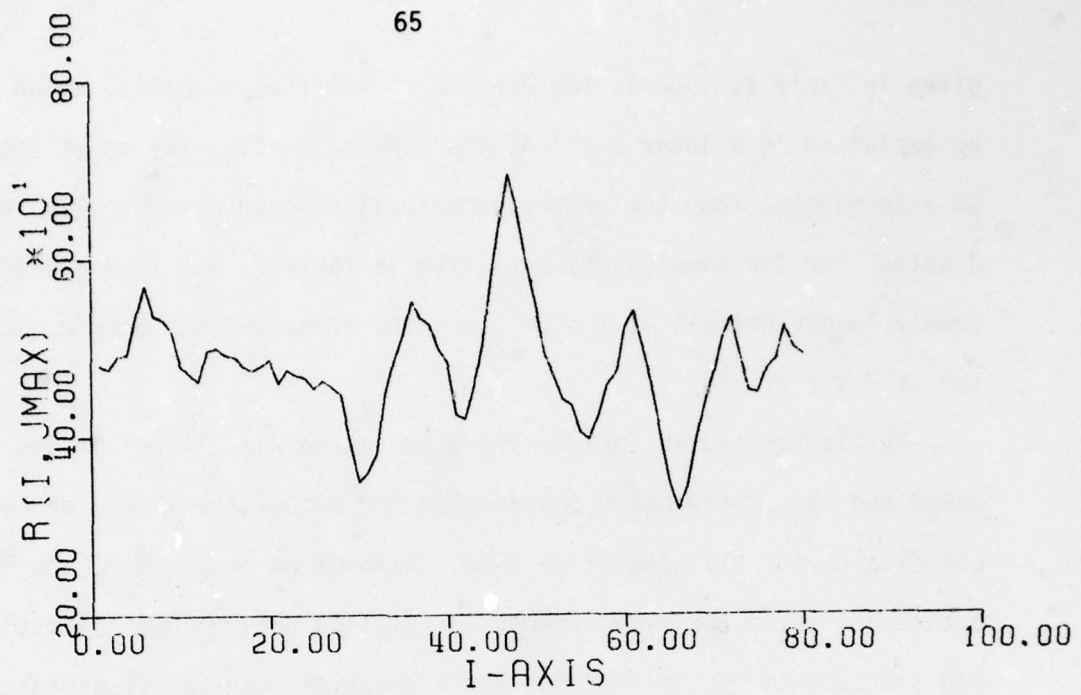
Figure 35. Cross-sectional plots of scene 4 correlation using the array average quantizer.

given in Table 2. Due to the dynamic response of the IRIS, which will be explained in a later section, the reduced HR-TV array is of size 50 x 28 pixels, thus the reference size is reduced considerably in the J axis. For the simulations presented in Table 2, the line average sample length was set at 7 pixels and the array average sample size was set at 7 x 7 pixels.

As illustrated in Table 2 there are large differences in the estimated and calculated match coordinates for either the I or J or both coordinates for all simulation runs. Also given in Table 2, and Tables 3 through 5, are the five highest correlation peak values. These values are included to see if the true match location occurred at a peak less than the maximum peak condition. There is only one case in Table 2 where this is possibly the situation. In the run for scene 4 using the array average quantizer, the fourth peak value possesses coordinates close to the estimated values. However, none of the other simulations show this tendency.

Because of the inability of the line average and array average quantizers to produce any valid TV-to-IR correlations for the simulations presented in Table 2, these preprocessors would not be viable canidates to be used for TV-to-IR correlation. It is possible though, that the average value preprocessors may produce better results when operating on characteristics of the image other grey scale differences. The results given in Table 2 and discussed above led to the use of the edge detector preprocessors for TV-to-IR correlation studies.

Scene	Quantizer	Est. IMAX	Cal. IMAX	Est. JMAX	Cal. JMAX	Peak Correlation Values					Ref. Size
						1st	2nd	3rd	4th	5th	
1	Line Avg. L = 7	26	28	53	75	494	484 I=26 J=76	480 I=50 J=73	475 I=52 J=72	472 I=89 J=102	32 x 20
	Array Avg. K = L = 7	23	10	55	102	391	391 I=69 J=50	391 I=80 J=25	387 I=77 J=25	387 I=82 J=24	32 x 20
4	Line Avg. L = 7	63	43	32	103	414	414 I=43 J=103	409 I=37 J=62	408 I=55 J=103	407 I=23 J=42	32 x 20
	Array Avg. K = L = 7	60	62	34	96	384	380 I=35 J=62	380 I=53 J=20	379 I=57 J=39	378 I=41 J=97	32 x 20

Table 2. Results of TV-to-IR correlations using the average value preprocessors.

D.   Results of the Standard Deviation Preprocessors

The third set of simulations attempted were those of TV-to-IR correlations using the standard deviation preprocessors. Table 3 shows the results of those simulations. Again the line sample length was 7 and the array sample size was 7 x 7. The 0 - 1 quantization threshold was set at 1σ above and below the average value. The results shown in Table 3 are very poor. In none of the simulations do the first five peak values show coordinates close to the estimated coordinates. There are a number of factors not illustrated in Table 3 which could effect the correlation results due to these preprocessors. These factors are: (1) sample size for the average value and standard deviation calculations; (2) proportionality constant, K, chosen for the $K\sigma$ quantization threshold; (3) size of the reference image. Due to time limitations, these factors were not studied thoroughly but should be considered in more deatil before the standard deviation preprocessors are eliminated for TV-to-IR correlation. The conclusion here is that from the results of Table 3 it is highly unlikely that the standard deviation preprocessors would be able to accomplish TV-to-IR correlation without considerably more study of the factors which effect the correlation function.

E.   Results of the Edge Detector Preprocessors

1. Simulation Results

Since the average value and standard deviation preprocessors exhibited poor performance for TV-to-IR correlation, a major portion of the work performed for this contract was involved in simulations for TV-to-IR correlations using the edge detector preprocessors. A number of tests

Scene	Quantizer	Est. IMAX	Cal. IMAX	Est. JMAX	Cal. JMAX	Peak Correlation Values					Ref. Size
						1st	2nd	3rd	4th	5th	
1	Line Std. Deviation SDK=1 L=7	26	90	53	69	210	205 I=88 J=69	203 I=37 J=49	202 I=77 J=70	201 I=64 J=70	16 x 20
	Array Std. Deviation SDK=1 K=L=7	23	26	55	45	263	260 I=66 J=35	259 I=32 J=37	258 I=71 J=34	255 I=69 J=34	16 x 20
4	Line std. Deviation SDK=1 L=7	33	42	32	7	208	195 I=12 J=22	194 I=91 J=101	192 I=22 J=70	192 I=98 J=44	16 x 20
	Array Std Deviation SDK=1 K=L=7	60	65	34	70	264	260 I=54 J=58	259 I=54 J=56	259 I=57 J=16	259 I=59 J=14	16 x 20

Table 3. Results of TV-to-IR correlations using the standard deviation preprocessors.

were carried out with edge detector preprocessors for the various scenes
given in section B of this chapter. The results of these tests are
given in this section.

In Table 4 the results of tests using scenes 1 and 4 show some
preliminary results obtained with the edge detector preprocessors. In
Tables 4 and 5, TVGTH refers to the gradient threshold used to convert
the HR-TV gradient image to a binary image and IRGTH is the threshold
value used for the IRIS image. Run numbers 1 and 2 of Table 4 were
made to show the effect of reference size on the shape of the correlation
surface. Figure 36 shows the cross-sectional plots of the correlation
surface for Run No. 1. At the time of this simulation the wide side
peaks in the J-axis cross section caused some concern. The scene for
this run was reviewed and it was found that the particular reference
chosen contained a large area of zeroes. It was felt that the large
area of zeroes were matching similar zero areas to the left and right
sides of the NASA tower in the IR edge image. To check this effect the
reference image was reduced to a size of 16 x 20 which contained approxi-
mately half one values and half zero values. It was reasoned that if
the matching on the zeroes was occurring then the side peaks should be
reduced considerably. Figure 37 shows the cross-sectional plots for
this test. A comparison of Figures 36 and 37 shows that the wide side
peaks in the J-axis completely disappear and the sharpness of the peak
in the I-axis plot was improved. This test confirmed the above specula-
tion and also gave the first clue as how to select the zero-one thresh-
old for the HR-TV gradient image. Runs 3 and 4 were made to see if the
correlation function would track a displacement made in the selection of

Scene	Run No.	Quantizer	Est. IMAX	CAL IMAX	Est. JMAX	CAL JMAX	Peak Correlation Values					Ref. Size
							1st	2nd	3rd	4th	5th	
1	1	2 x 2 TVGTH = 30 IRGTH = 30	27	28	56	57	511	506 I=11 J=97	505 I=31 J=10	505 I=34 J=11	504 I=25 J=19	32 x 20
	2	2 x 2 TVGTH = 30 TVGTH = 30	27	28	56	56	214	205 I=67 J=58	204 I=25 J=10	204 I=94 J=39	202 I=45 J=40	16 x 20
	3	3 x 3 TVGTH = 100 IRGTH = 100	32	35	56	57	547	544 I=35 J=62	542 I=34 J=44	542 I=35 J=59	538 I=37 J=62	32 x 20
	4	3 x 3 TVGTH = 100 IRGTH = 100	26	31	56	57	524	504 I=29 J=45	501 I=32 J=62	493 I=27 J=44	493 I=30 J=62	32 x 20
4	5	2 x 2 TVGTH = 30 IRGTH = 19	55	55	32	31	410	407 I=61 J=94	406 I=55 J=29	403 I=67 J=48	402 I=61 J=68	26 x 26
	6	2 x 2 TVGTH = 30 IRGTH = 29	55	67	32	42	379	378 I=55 J=29	377 I=55 J=31	376 I=61 J=77	373 I=58 J=19	26 x 26
	7	2 x 2 TVGTH = 30 IRGTH = 39	55	55	32	29	356	354 I=67 J=93	352 I=58 J=20	348 I=61 J=75	348 I=64 J=72	26 x 26

Table 4. Results of TV-to-IR correlations using the edge detector preprocessors on scenes 1 and 4.

Scene	Run No.	Quantizer	Est. IMAX	CAL IMAX	Est. JMAX	CAL JMAX	Peak Correlation Values					Ref. Size
							1st	2nd	3rd	4th	5th	
4	8	3 x 3 TVGTH = 145 IRGTH = 74	55	55	31	31	446	431 I=55 J=28	430 I=61 J=65	427 I=67 J=88	426 I=64 J=73	26 x 26
	9	3 x 3 TVGTH = 145 IRGTH = 84	55	55	31	31	434	424 I=55 J=28	423 I=64 J=73	418 I=55 J=42	414 I=67 J=86	26 x 26
	10	3 x 3 TVGTH = 145 IRGTH = 94	55	55	31	29	423	421 I=55 J=31	421 I=64 J=72	414 I=61 J=70	412 I=64 J=78	26 x 26

Table 4. (Continued)
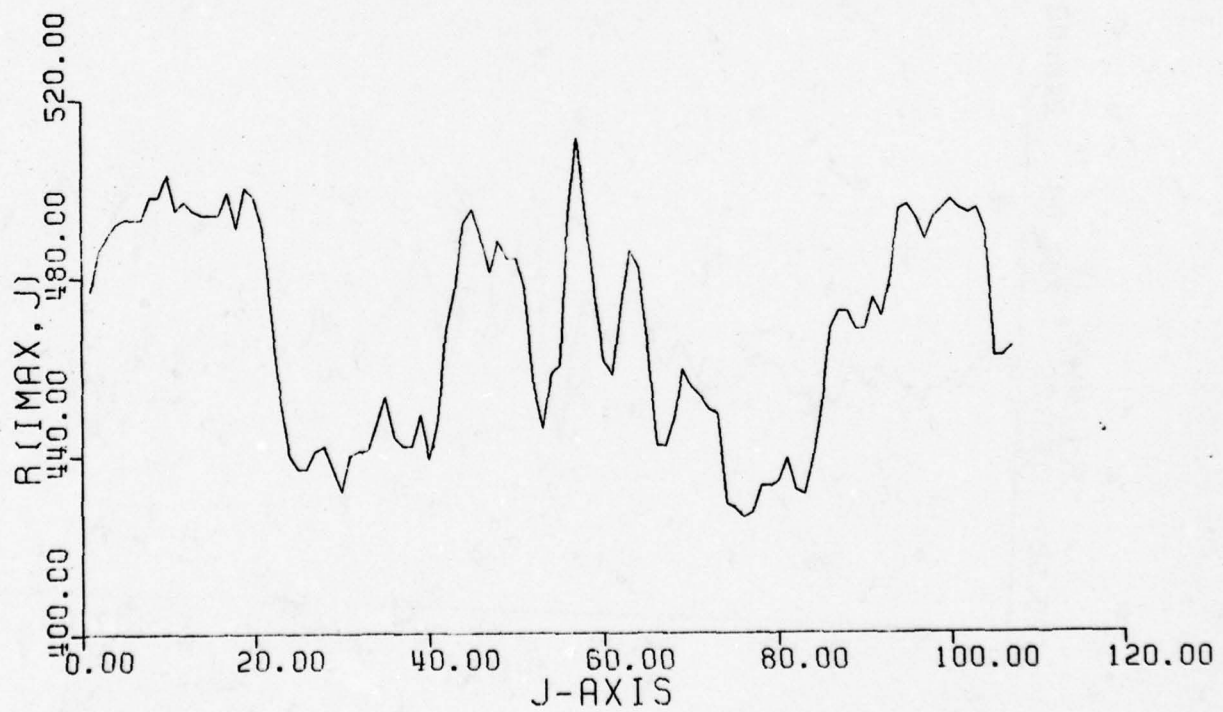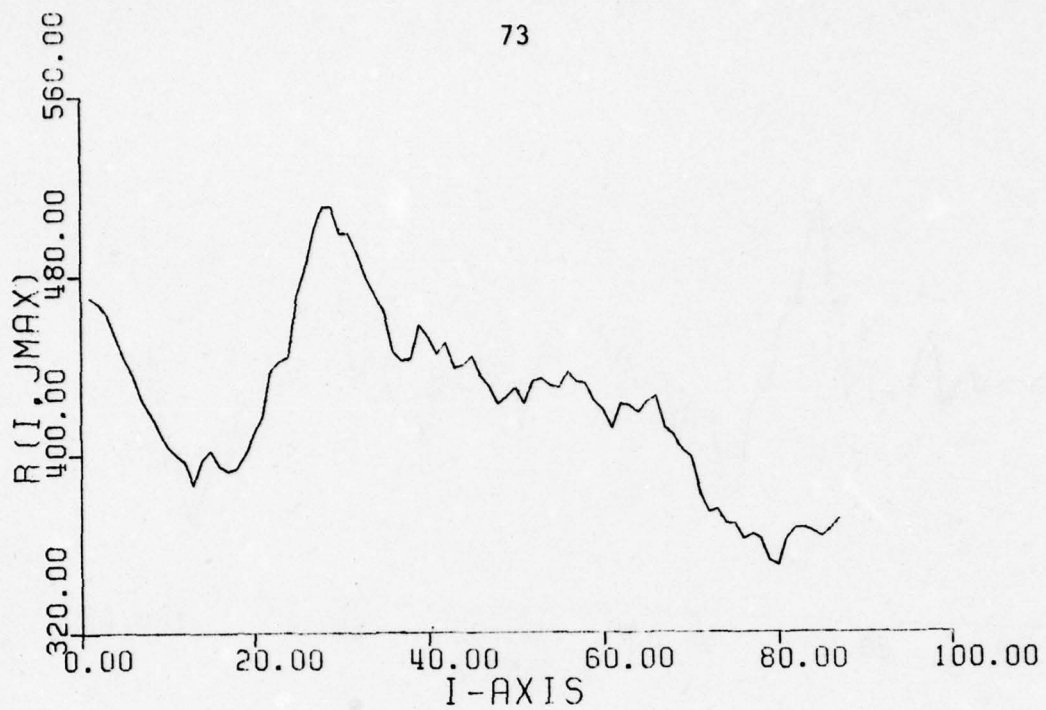
Figure 36.   Cross-sections of Run 1 - Table 4 through
the maximum value.
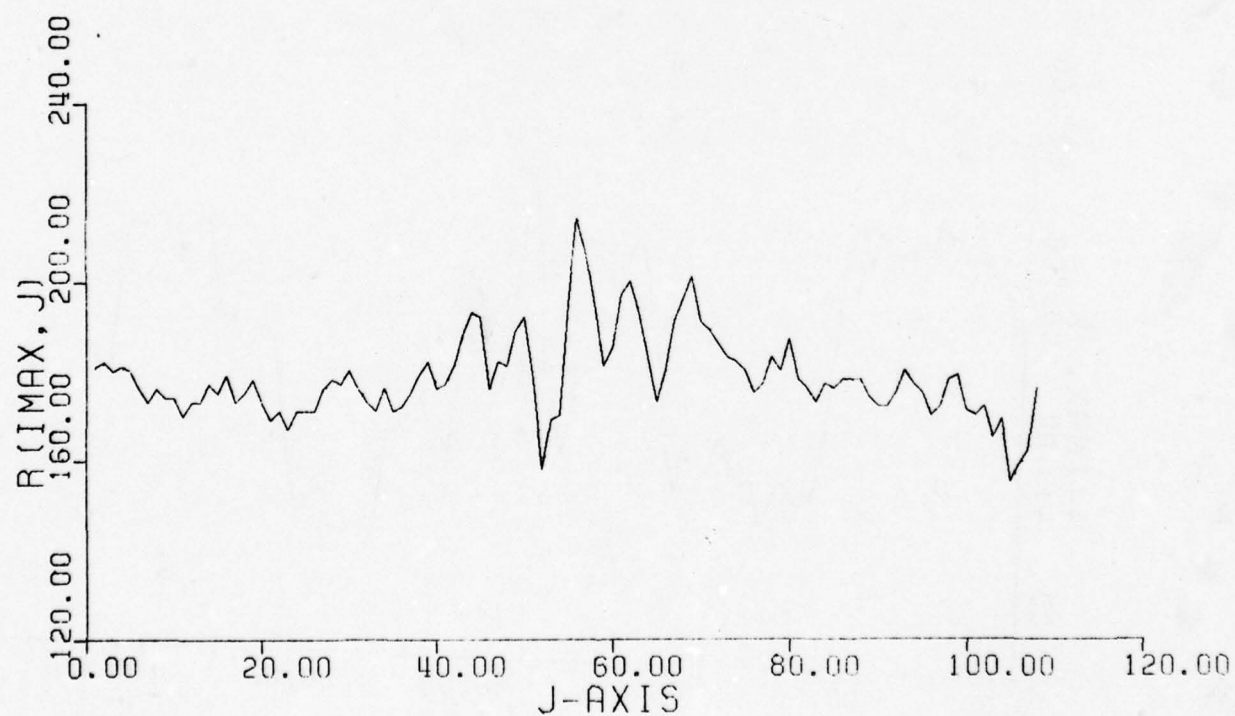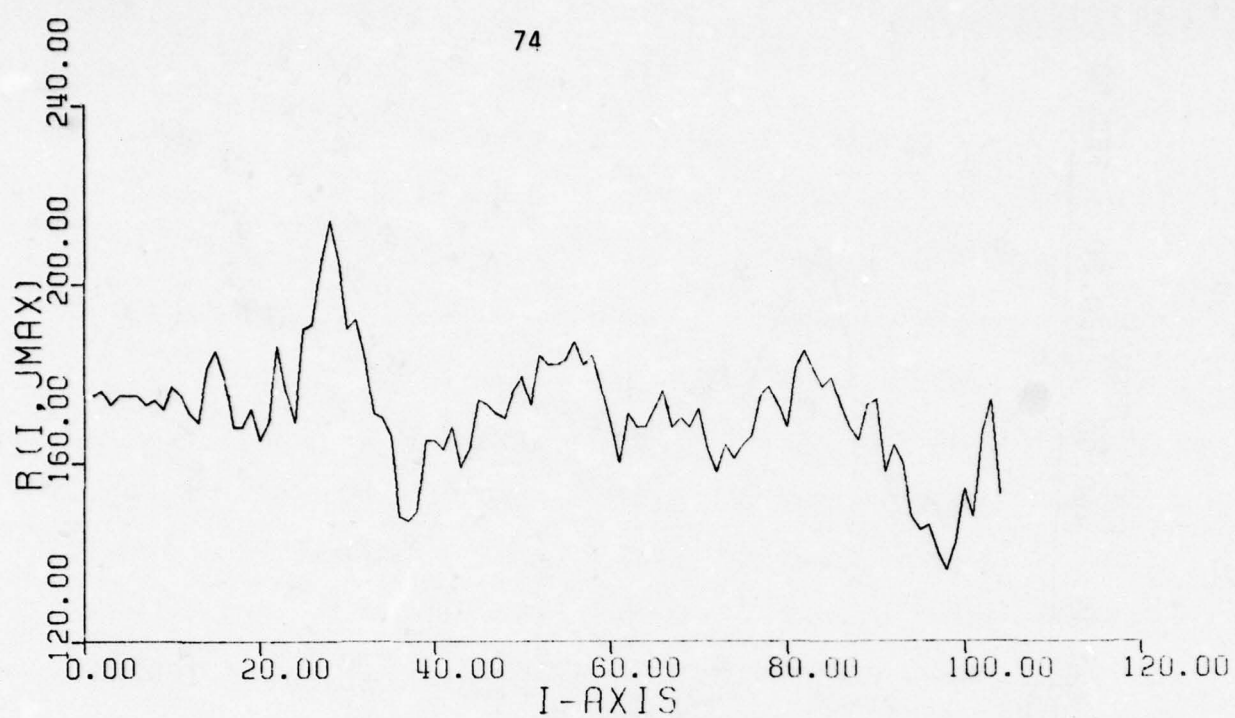
Figure 37.   Cross-sections of Run 2 - Table 4
through the maximum value.

the reference image. As shown by the estimated IMAX coordinates the reference was displaced by 6 rows in the two runs. The calculated IMAX coordinates reflect a change of 4 rows with no change in the JMAX coordinates.

Runs 5 through 10 or Table 4 were made to illustrate the effects of changing IRGTH. The gradient threshold used for the HR-TV image was set to yield approximately an equal distribution of 1's and 0's in the reference. Run 6 shows that a false peak situation did occur, while the second and third peak correlation values illustrate true match conditions for this simulation.

Runs 5 through 10, excluding run 6, also give an indication as to the reliability of the 2 x 2 and 3 x 3 edge detection algorithms. The reliability of these algorithms is illustrated by the difference in magnitude of the true correlation peak and the second and third peak correlation values. The difference in successive peak correlation values with the first due to the 3 x 3 edge detector are much larger than those produced by the 2 x 2 edge detector. Due to this fact, a false correlation peak would less likely occur when using the 3 x 3 edge detector, but erroneous edge points caused by noise in the image could possibly cause false correlation peaks when using the 2 x 2 edge detector. As shown in section B of this chapter the 3 x 3 edge detector tends to widen edges in the image which causes a smoothing effect on the edge points due to stray noise. The 2 x 2 edge detector does not exhibit edge point smoothing and edge points caused by noise would propagate through the correlation system.

Table 5 shows the simulation results for tests made on scenes 6 and 7. In these runs the reference array was extracted from three different row coordinates in the complete HR image. In each case the HR-TV threshold remained constant and IRGTH was adjusted to yield the highest correlation value. The process for adjusting the IRIS threshold will be explained later. As can be seen from Table 5 the results indicate good correlations in most runs. Run 4 shows a multiple peak correlation value. The first and second peak correlation values are equal in magnitude, one indicating proper match coordinates and the other a false peak condition. A slight adjustment of IRGTH would probably rectify this result.

In this section the results of a number of correlation simulations have been presented which show that TV-to-IR correlation can be accomplished using edge detection algorithms for a number of different scenes. However, there were cases in which correlations were attempted and no favorable results could be obtained. Scene 5 is one example. The edge plots produced for the HR-TV and IR images showed very little resemblance. Correlations were attempted with very poor results. The overall conclusion from all the simulations was that edge detection preprocessing of the video did lead to correct correlations most of the time whereas other algorithms failed most if not all of the time. It was also concluded from the simulations that proper selection of the gradient threshold is critical. Methods to select the gradient thresholds are discussed in the next section.

2. Determination of the Gradient Threshold for the HR-TV Image

From a study reported in [5], it was determined that the quantized HR-TV reference image should contain an equal number of edge points (1's)

Scene	Run No.	Quantizer	Est. IMAX	CAL IMAX	Est. JMAX	CAL JMAX	Peak Correlation Values					Ref. Size
							1st	2nd	3rd	4th	5th	
6	1	3 x 3 TVGTH = 82 IRGTH = 70	55	55	56	56	432	418 I=54 J=54	404 I=55 J=52	403 I=42 J=24	403 I=57 J=62	26 x 26
	2	3 x 3 TVGTH = 82 IRGTH = 46	50	50	56	56	438	434 I=50 J=42	425 I=52 J=82	424 I=10 J=43	423 I=43 J=25	26 x 26
	3	3 x 3 TVGTH = 82 IRGTH = 114	60	59	56	56	463	448 I=56 J=22	448 I=57 J=50	445 I=59 J=52	442 I=51 J=22	26 x 26
7	4	3 x 3 TVGTH = 194 IRGTH = 194	61	61	47	47	440	440 I= 1 J= 7	427 I=10 J=42	427 I=58 J=33	426 I= 1 J=17	26 x 26
	5	3 x 3 TVGTH = 194 IRGTH = 144	57	57	47	46	432	417 I=52 J=55	413 I=52 J=48	412 I=67 J=19	410 I=60 J=15	26 x 26
	6	3 x 3 TVGTH = 194 IRGTH = 220	65	65	47	47	401	397 I= 1 J=98	392 I= 8 J=25	391 I= 1 J=80	391 I= 5 J=16	26 x 26

Table 5. Results of TV-to-IR correlations using the edge detector preprocessor on Scenes 6 and 7.

and nonedge points (0's). The ratio of 1's and 0's in the reference

image is dependent on the value of gradient threshold selected. Figure

38 is a rough plot which demonstrates how the number of 1's and 0's in

the reference image vary with threshold. As the plot indicates a 50-50

mix of 1's and 0's can be obtained if the median gradient value of the

generated HR-TV gradient array is used as the threshold. The above

requires storage of the gradient array to identify the median gradient
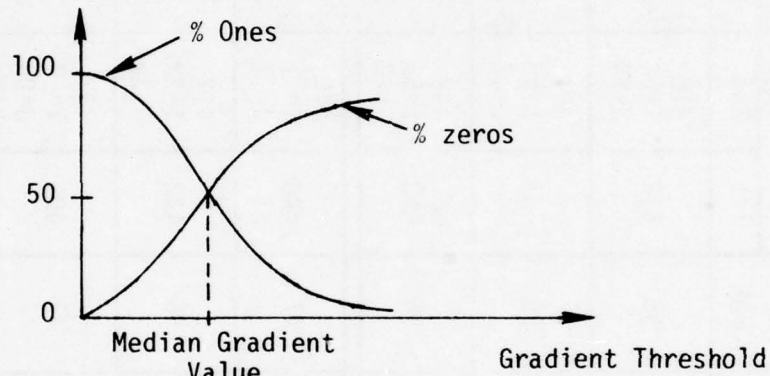
Figure 38. 1-0 Distribution vs. Threshold

value. Then quantization of the gradient array could proceed. This

method of theshold selection for the reference image was used for a

number of the simulations given in Tables 4 and 5 with favorable results.

3. Determination of the Gradient Threshold for the IRIS Image

In order to determine the best or optimum threshold to be used for

the IR image a number of simulations were made by these investigators and

by the investigators as reported in [5] to study the sensitivity of the

correlation peak to IR threshold. The optimum threshold is defined as

that which yields the highest correlation value given a fixed reference

image. Figure 39 is a plot of maximum correlation values vs. threshold
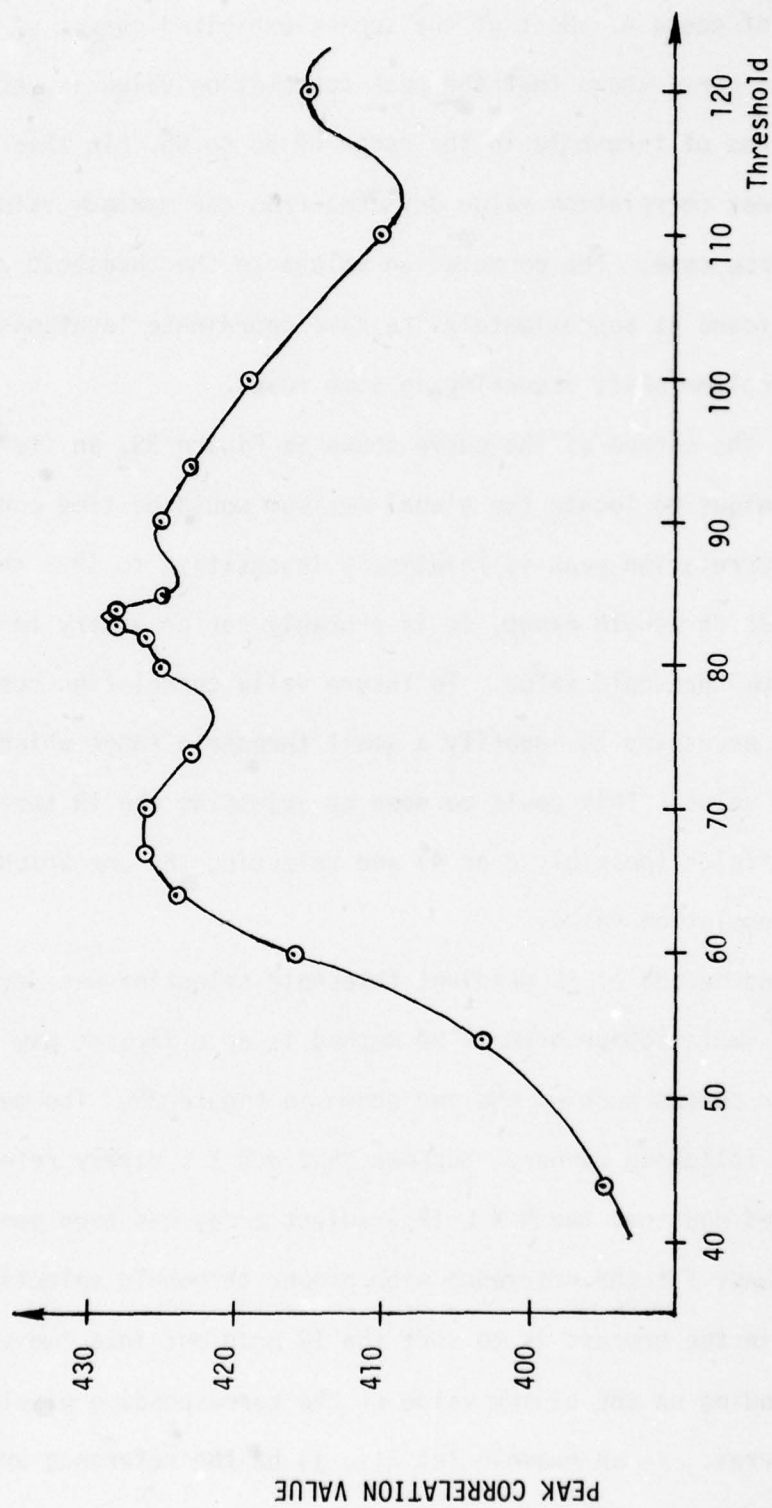
Figure 39. Peak correlation value vs. IRIS threshold for scene 4 - parking lot.

using data of scene 4. Most of the scenes exhibited curves of the same
shape. This curve shows that the peak correlation value is very insensi-
tive to values of threshold in the range of 65 to 95. In this threshold
range the peak correlation value deviates from the maximum value by only
5 in the worse case. The correlation values in the threshold range 65
to 95 were found at approximately the same coordinate locations, with
only a two-column shift occurring in some cases.

Due to the nature of the curve shown in Figure 39, an iterative
search technique to locate the global maximum would be time consuming.
Since the correlation peak is relatively insensitive to IRIS threshold
within a wide threshold range, it is probably not necessary to find an
exact optimum threshold value. To insure valid correlation results it
may only be necessary to identify a small threshold range which contains
the optimum value. This could be done by adjusting the IR threshold in
successive fields (possibly 3 or 4) and selecting the one which gives
the peak correlation value.

A second method of IR gradient threshold selection was developed for
use in the simulation program. The method is an efficient way to generate
the data for curves such as the one shown in Figure 39. The method oper-
ates in the following manner. Suppose that a K X L binary reference has
been selected and that the K X L IR gradient array has been generated
which will best fit the reference with proper threshold selection. The
first step in the process is to sort the IR gradient into two vector
arrays depending on the binary value of the corresponding pixel in the
reference array. As an example let $X(i, j)$ be the reference array value

of pixel (i, j). Let Y(i, j) be the IR gradient value of pixel (i,j).
Then

YONE (I) = Y(i, j) if X(i, j) = 1 and

YZERO (I) = Y(i, j) if X(i, j) = 0

where YONE(·) and YZERO(·) are vector arrays of appropriate IR gradient
values. The next step is to place YONE(·) and YZERO(·) in ascending
order of magnitude. The minimum and maximum gradient values among the
two vector arrays are identified as limits for the range of gradient
threshold. Starting with the minimum gradient value the threshold is
now varied throughout its range. To determine the resulting correlation
estimate for a given threshold value, the YONE(·) and YZERO(·) arrays
are searched. Those values equal to and above the threshold in the
YONE(·) array would yield 1 - 1 (Ref to IR) matches and those values
below the threshold in the YZERO(·) array would yield 0 - 0 matches.
Therefore, the process of estimating the correlation values as the
threshold is varied is one of keeping track of the number of 1 - 1 and
0 - 0 matches in the YONE(·) and YZERO(·) arrays. Figure 40 describes
the process graphically, where YONE(·) and YZERO(·) have been ordered.
The process continues by setting the threshold at the next highest
gradient value among the two arrays. Once all threshold values have been
set, the threshold value yielding the highest correlation value is selected
as the optimum. The optimum threshold value insures the best fit of the
IR binary array to the given binary reference array. This method, while
not practical for real time implementation, has been of great benefit for

YONE(·)   YZERO(·)

of
1-1 matches

Threshold (Th)

Threshold (Th)

of
0-0 matches
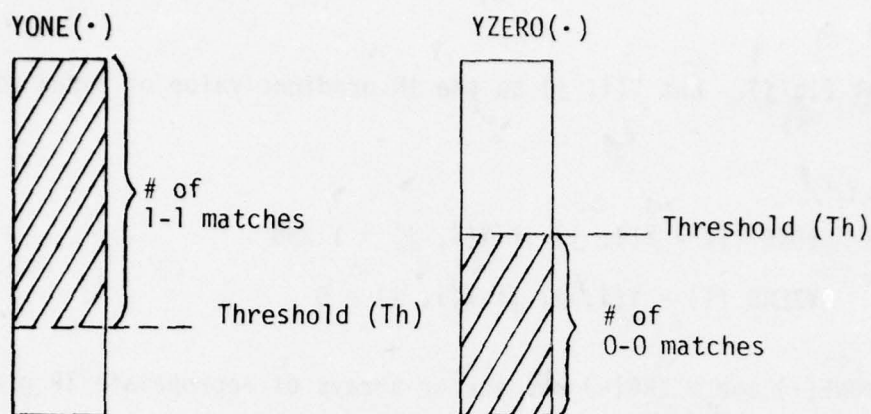
R(Th) = (# of 1-1 matches) + (# of 0-0 matches)

Figure 40.   Graphical representation of IR
gradient threshold selection method.

simulation purposes in getting a quick idea of where to set the IR

gradient threshold for correlation simulations.

F. Difficulties Encountered in the Simulation Process

During the course of running the simulations reported on here, a

number of difficulties were encountered. This section lists those diffi-

culties and explains the methods by which they were rectified.

1. Scale Factor determination between HR-TV and Sensor Images

In the first simulations attempted for TV-to-TV and TV-to-IR

correlations is was suspected that small errors in the horizontal and

vertical scale factors for HR-TV resolution reduction was affecting the

goodness of the correlation function. Therefore, it was decided that a

scale factor sensitivity analysis be made for these two types of correla-

tions. The results of those studies will now be presented.

a. TV to TV Correlation Scale Factor Sensitivity

A number of simulation runs were made to determine the optimal scale factor reduction for high resolution TV to low resolution TV correlation. The simulations used a line average quantizer which set each pixel to 0 or 1 based on whether its value was below or above the average value of the previous eleven pixels. The reference image in each case was 31 by 31 pixels which would limit the maximum correlation surface value to 31 squared or 961.

Table 6 gives the results obtained using scene 1 which is the NASA building with a crane and antenna on its roof. From the table it is obvious that the optimum scale factor for the HR-TV to LR-TV correlation is 4 to 1 in both axes. Although Table 6 does not show any results for different scale factors in the two axes (e.g., 3.8 in vertical axis and 4.0 in horizontal axis), simulations were run with the result that the

Scale Factor Vertical X Horizontal	RMAX	IMAX	JMAX
3.6 x 3.6	639	33	21
3.8 x 3.8	639	33	21
4.0 x 4.0	644	30	25
4.2 x 4.2	638	34	20
4.4 x 4.4	634	32	23

Table 6. Scale factor sensitivity analysis - Scene 1

4.0 scale factor reduction in each axis is optimal. The variation in the values of the row and column at which the peak occurs is caused by the fact that as the scale factor is changed, the location of the chosen

reference within the FOV changes. The peak in each case was well defined and located at the predicted value.

Table 7 gives the results of the same analysis using scene 3 which is a wooded area. Although the peak at a 4.0 by 4.0 reduction factor was low, it is felt that this was caused by a slight shift in the reference. If one considers all of the data points in Table 7, the optimal value appears to be 4.0 by 4.0 which was the expected value from the HR and LR TV specifications. The sharpness of the peaks (an indication of the quality of the peak) was best for the 3.8 x 3.8 and 4.0 x 4.0 scale factors.

		Horizontal Scale Factor			
V e r t i c a l S c a l e F a c t o r		3.6	3.8	4.0	4.2	4.4
	3.6	RMAX = 593				
	3.8		RMAX - 618	RMAX = 601		
	4.0		RMAX = 616	RMAX = 604	RMAX = 605	
	4.2			RMAX = 609	RMAX = 618	
	4.4					RMAX = 606

Table 7. Scale factor sensitivity analysis - Scene 3

b. TV-to-IR Correlation Scale Factor Sensitivity

A number of simulation runs were made to determine the optimal scale factor reduction for high resolution TV to IR correlation. The simulations used the 2 x 2 Roberts Cross Operator with preset thresholds to create the binary images. Two sets of simulations were run. The first used a reference size of 32 x 20 which limits the maximum correlation surface value to 640 and the second set used a reference size of 16 x 20 which would limit the maximum correlation surface value to 320. The 16 x 20 reference was also used to remove the wide side peaks as discussed in section E of this chapter.

Tables 8 and 9 give the results obtained using scene 1 which is the NASA building with a crane and antenna on its roof. Although the peak

Horizontal Scale Factor	RMAX	IMAX	JMAX
16	505	34	11
17	505	28	57
18	511	29	57
19	511	29	57
20	505	16	101

Table 8.   Horizontal scale factor sensitivity analysis with vertical scale factor equal to 4.722 - Scene 1

at a 4.722 x 18.0 (Vertical x Horizontal) reduction factor is lower than some of the others it is felt that these are the optimum scale factors when one considers sharpness of the peaks and the ratio of peak values to the false peaks in both axis cross-sections.

Vertical Scale Factor	RMAX	IMAX	JMAX
3.5	502	28	57
4.0	506	29	57
4.5	517	30	57
4.722	511	29	57
5.0	520	29	57
5.5	524	29	57

Table 9.   Vertical scale factor sensitivty analysis
with horizontal scale factor equal to 18.0
Scene 1

The results using a 16 x 20 reference supported the conclusions

made above.   Only the vertical scale factor was changed in these runs.

Again the results for a vertical scale factor of 4.722 was optimum.

2.   Sampling Rate for the IRIS Video Due to the Dynamic Response of the
IR Sensors

Each field of video consists of 240 lines with each line sampled to

512 pixels yielding a 240 x 512 array for each field.   Each line consisted

of all of the active video and a small part of the horizontal retrace.

Since the field rate is 60 Hz, the video sampling rate is approximately

10 MHz.

When the edge detection algorithms were first applied to the IRIS

video, it was noticed that very few vertical edges were present in scenes

that were known to have vertical edges such as the NASA building.   The

reason for this is that the rate of change of the video along a line is

dependent on the instantaneous horizontal field of view of the IRIS

detectors and their dynamic response. In other words by oversampling and using the Robert's two-by-two edge detection algorithm, vertical edges were not being detected.

This phenomena can be explained by considering the characteristics of the IR detectors. The response time of the IR detector is 420 ns. If the detector is modeled as a first order lag, its transfer function is given by

$$\frac{V_{out}}{V_{in}} = \frac{1}{TS+1} = \frac{1}{.42s+1} = \frac{1}{1+s/2.38}$$

where the time constant, T, is in microseconds.

An edge in the video would appear as a step input signal (A/s). The rise time of the detectors, however, determine the speed of the response. Figure 41 shows that with a detector time constant of 420 ns, sampling the video at approximately 10 MHz yields approximately four samples per time constant. This illustrates why even an abrupt edge is not very predominant in an edge detection algorithm.
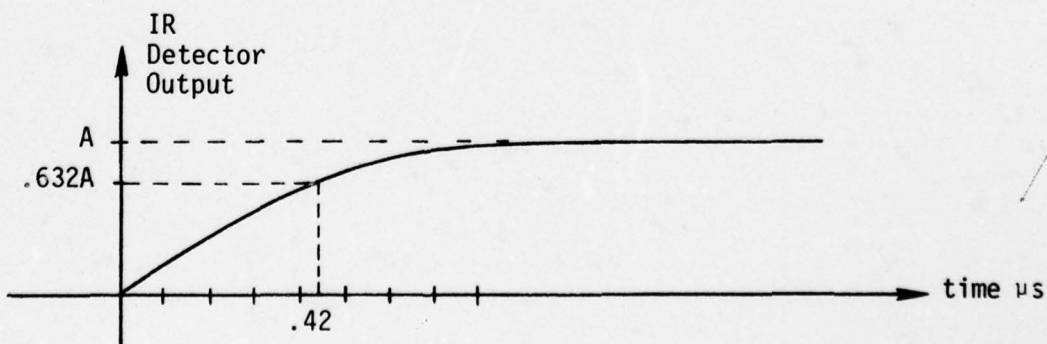
Figure 41. IR detector response to an edge.

The above results led to the conclusion that even though the original video was sampled at approximately 10 MHz, only every fourth sample should be used thereby reducing the effective sampling rate to approximately 2.5 MHz. Simulations showed that correlation was impossible using every sample (10 MHz sampling rate) and not very good using every other sample (5 MHz sample rate) but was good using every fourth sample (2.5 MHz sample rate).

4. SENSORS AND STATISTICAL MODEL

In this section two subjects are treated. First a descriptive review of imaging sensor characteristics is given in terms of typical performance parameters and their inter-relationships. Secondly, further analysis of threshold statistics for the binary correlator is given which seeks to place the analysis on a more sound theoretical base and to include the very real possibility of pixel mis-match at registration due to sensor contrast reversals or geometric distortions. A continuation of previous work is presented which allows inclusion of pixel mis-match.

An area which is discussed only qualitatively is the effects expected when all pixels in an image cannot be considered independent. A quantitative treatment of these effects is strongly dependent on specific scene characteristics and was not done for the present effort. A quantitative analysis based on judiciously selected scene characteristics should be considered for further work.

In particular, the false alarm problem is typically analyzed based on an assumption of totally uncorrelated images. This gives the familiar error function type false alarm curve which is highly optimistic. A more realistic analysis is needed which includes the effects of spatial frequency content of the images and allows for practical cases where the correlation function has an inherent broad peak.

Else a fast algorithm for the phase correlation method should be sought. It has a much sharper inherent correlation peak.

A. Characteristics of Passive, Infrared,

Imaging Sensors

Performance characteristics for any electro-optical sensor, be it passive, active, imaging or non-imaging, are typically described in terms of a few selected parameters. This set of parameters, while not unique, typically includes a measure of signal-to-noise ratio, spatial resolution (or MTF), time response, spectral band, dynamic range, noise equivalent flux density (NEFD), etc. Additionally other related parameters or application specific parameters may be defined for a given system.

Although some understanding of the effect of these parameters is achieved from their definitions, a more complete understanding requires a detailed parametric analysis. This is complicated by the fact that many parameters exhibit a complex interactive dependence on more than one element of the total system. Additionally, it is necessary to include parameters which exhibit both radiometric and electrical properties. The necessary conversions from radiometric to electrical quantities are typically given in terms of responsivity of the photodetector. Also, the system noise includes several possible sources dependent on the specific sensor design.

Rather than bog down in the detailed analysis of a specific sensor design, the following discussion will be limited to fundamental concepts which have general application. These concepts are best discussed in terms of the following sub-categories.

- Scene characteristics

- Geometry effects

- Optical path

- Ambient radiation characteristics

• Optics (lenses, mirrors, optical filters, baffle design)

• Photodetector

• Imaging mechanism

• Electronics

The concepts are discussed in terms which hopefully convey physical understanding instead of terms which give detailed parametric equations. The latter can be provided but would require in-depth study for understanding.

1. Scene Characteristics

Except for certain coherent or selective radiators, the radiation from a typical scene consists of two components: 1. emitted thermal radiation dependent on scene emissivity and temperature profiles, and 2. reflected radiation dependent on the scene reflectivity and its ambient radiation environment (typically sunlight). Normally for wavelengths of interest, the viewed scene can be assumed to be opaque (transmissivity = 0). The resultant combined radiation characteristics provide a spectral signature for a given scene. This spectral signature is one of the major inputs to a sensor design analysis.

Spectral signatures can be determined in a number of ways including:

Experimental - fortunately data are available for radiation properties of a large number of materials and specific target compositions (experimentally measured). Unfortunately these data are often scattered through various references and, more importantly, often measured under conditions which do not match the intended application scenario.

Theoretical - requires assumptions (basically simplifying) about the spectral dependence of target emissivity, reflectivity and ambient

environment as well as about expected target temperature and cross-section. The advantage of this technique is that ball park figures are easily obtained and modified.

Hybrid - basically employs the simplicity of the theoretical approach but uses experimental data for the more common and easily found radiation properties.

2. Geometry Effects

Most objects within a scene can be assumed to be diffuse emitters/ reflectors with isotropic radiation properties. This assumption is usually made in propagating the spectral signature from the scene to the sensor (results in a $1/R^2$ reduction in radiance level). Other geometry effects have to do with the size and signal strength of an object within the field-of-view projected onto the photosensor. For example a target subtends a total solid angle at the sensor given by the ratio of target area to range squared. This information is useful in determining the percentage of the total sensor field-of-view occupied by the target. Further, signal strength on the photodetector increases as the primary optical area increases. That is, the collecting solid angle of the primary optics for the sensor is given by the ratio of optics area to range squared.

3. Optical Path

For free space propagation the target characteristics and geometry effects are sufficient to determine the radiant signal levels on the photo-surface. However, for propagation through the atmosphere or any other refracting medium consideration must be given to 1. radiance reduction through absorption or scattering out of the sensor field-of-view, 2. radiance increases through scattering of background radiance into the sensor

field-of-view, and 3. wavefront distortion due to turbulence effects. Effects 1. and 2. tend to reduce the contrast within the image. Effect 3. causes a blurring effect whose time averaged result is a reduction in resolution of the image. The first two affect signal level; the third affects MTF.

4. Ambient Radiation Characteristics

For typical imaging applications, the ambient radiation environment includes incident and reflected sunshine, incident and reflected earthshine (significant at longer wavelengths), earth limb or airglow and possible high radiance sources not in the field-of-view. Depending on the spectral region of interest and the specific application, various elements of the ambient radiation environment represent either signal or noise to the sensor. *Ideally, the sensor "sees" only the intended target area through* a perfectly clear optical path with no extraneous radiation entering the *sensor.* Methods for improving the sensor's ability to accomplish the ideal objective include judicious selection of spectral band, optical filtering to exclude wavelengths of no interest, optical design and baffle design to essentially trap unwanted stray radiation. Even with the best application of these methods there will be some stray radiation in the detector field-of-view which cannot be eliminated.

5. Optics

As mentioned above the optical design has as one goal, the optimum collection of scene radiation and rejection of stray radiation. Additionally, the optics must provide image magnification where needed, minimuze distortion and aberrations from the optical elements, and provide transmission characteristics consistent with the desired spectral band of sensitivity. The

1.0

1.1

1.25

4.5
5.0
5.6
6.3

2.8
3.2
3.6
4.0

1.4

2.5

2.2

2.0

1.8

1.6

MICROCOPY RESOLUTION TEST CHART
NATIONAL BUREAU OF STANDARDS-1963-A
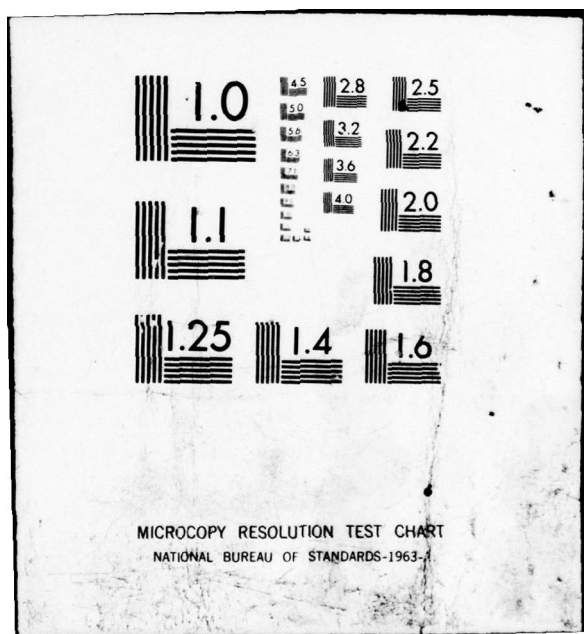
optics in conjunction with detector size, target area size and sensor-to-target range determine the sensor field-of-view and basic resolution.

6. Photodetector

Photodetectors are a class of optical detectors, consisting of several different types, whose electrical properties are modified through the absorption of discrete quanta of optical energy, or photons. This absorption results in ionizations which produce charge carriers. In contrast, thermal detectors absorb optical radiation resulting in increased lattice vibration. These lattice vibrations show up in temperature dependence of the detector electrical properties.

The photodetector is the heart of any sensor and effectivity determines the signal-to-noise ratio, time response and dynamic range of the sensor. The photodetector is characterized by several parameters and functions including responsivity, time constant, detectivity and size.

Responsivity is a measure of the detector's ability to convert optical radiation into an electrical signal. It typically has units of volts/watt or amps/watt. Responsivity is dependent on wavelength, detector operating temperature and frequency. Further, the dependence on these three parameters is inter-related. Obviously, in choosing a detector for use in a sensor design, the detector should have high responsivity at the dominant wavelengths in the scene spectral signature.

Time constant for a photodetector is dependent on the mean lifetime for photo-generated charge carriers. This carrier lifetime is a complex function of detector type, dopant material, physical size and detector temperature. These characteristics as well as responsivity and other photodetector

performance curves must be provided by the manufacturer. An additional factor which affects time response and detectivity is the level of total irradiance on the detector, including both scene and stray radiation plus any thermal radiation from the sensor optical elements. A reasonably simple model can be devised to show how time constant depends on the above parameters.

Detectivity is a measure of how sensitive a photodetector is; a large detectivity is good. An equivalent performance measure often used, which is just the reciprocal of detectivity, is NEP or noise equivalent power (measured in watts). The NEP gives the incident radiant power level in watts which will produce a unity signal-to-noise ratio out of the detector. The output signal and noise levels depend upon the detector area and the electronic bandwidth of the detector circuitry. Thus NEP is not a very good comparison parameter unless the detector size and bandwidth effects are accounted for. This is done by defining a specific detectivity, called D*, which is normalized to a detector area of one square centimeter and a noise bandwidth of one Hertz. Curves of D* versus wavelength are often used to compare various detectors. Further, D* depends on total incident radiation level frequency and exhibits a threshold dependence on detector temperature.

A performance measure which characterizes the entire sensor including all elements from the optics through the electronics is the sensor NEFD or noise equivalent flux density. NEFD is the level of incident radiant flux (in watts/m^2) on the sensor which produces a signal-to-noise of unity. Thus it is similar to NEP except for the units and is easily related to sensor signal-to-noise ratio. For example we have S/N = E/NEFD where E is the

scene produced irradiance level at the sensor (depends only on the scene and path characteristics) and NEFD is dependent only on sensor parameters. Analysis of how various sensor parameters affect NEFD is a useful design tool.

The effect of detector size, in addition to those effects already discussed, is to limit the system spatial resolution. As a rough first estimate, the limiting resolution can be taken to be the instantaneous field-of-view in each direction subtended by the detector. This is the ratio of detector width or length to the effective focal length of the optical system. Some enhancement of this spatial resolution can be achieved electronically. The electronics is then said to provide an MTF boost to the overall system resolution. For total system resolution it is usually convenient to represent each element of the system by an appropriate MTF or modulation transfer function and take the products to get the total.

7. Imaging Mechanism

For point detectors imaging is accomplished by scanning the detector field-of-view across the scene to be imaged. This scanning is typically accomplished mechanically, either with rotating or mutating mirrors or with gimbals. Requirements on the mechanical scanning can be relaxed by using either linear or two-dimensional arrays of detector elements. CCD and CID arrays of photodetectors are now available for a few wavelength regions. Of course, the price paid for using arrays of photodetectors is increased electronics complexity plus the possibility that some elements in the array will be defective.

Area detectors such as used in Vidicons and other TV type sensors achieve scanning and readout with an electron beam. This has advantage of

simplicity but is less rugged than solid state photosensors.

8. Electronics

The electronics must drive the scan mechanism, amplify and process the signal. For longer wavelength infrared systems, the first amplifier stage is also a significant source of noise. Typically, both the detector and preamplifier are cooled to reduce thermal noise. For systems operating in the visible region, noise is much less of a problem because of the availability of higher D^* detectors and because fewer thermally generated carriers will exist in a detector whose energy bandgaps represent visible wavelengths. Thus cooling is not usually required for visible wavelengths.

As already mentioned, the electronics can boost system resolution and can be used to further process the signal for utilization.

In summary, the above descriptive discussion has introduced many of the primary parameters affecting a sensor design or analysis. Dynamic range is determined by the photodetector characteristics and is the range of linear responsivity. The lower end is limited by the detector NEP and the upper end is limited by the irradiance level at which the detector saturates. Saturation occurs when no further charge carriers can be generated and is a function of the detector materials, doping levels and other detector characteristics. Dynamic range can be extended by the sensor in steps by optical attenuation of the incoming radiation. The lowest end is, however, still that determined by NEP.

B. Statistical Model for Threshold Analysis

An analysis for determination of probability of correct registration (P_d) and probability of false registration (P_F) as functions of choice of

threshold, image signal-to-noise ratios and image statistics was done for correlation of two binary quantized TV images. Results of this analysis are given in [4] and further developed in [6]. This analysis was based on two simplifying assumptions: 1. The images experienced no geometric distortion and 2. all the pixels across an image were statistically independent. Further, since the correlation was done for like images (both from TV visible spectrum sensors) it was assumed that at registration, the images were identical except for additive noise terms.

In the context of the present task of correlating TV with FLIR images the assumption of identical images at registration can no longer be made. Additionally, there is greater likelihood that geometric distortion will be present. These modifications to the statistical model were examined for a binary TV to FLIR correlator.

In addition, a re-evaluation of the statistical properties for a binary correlator were examined in terms of "measure of goodness" for estimates of statistical functions. The correlation estimate was found to be both unbiased and consistent with a variance proportional to one over the number of data points (KL) for the distortionless case. It was further verified how the estimate variance is scene dependent.

1. Statistical Analysis Theory

In re-evaluating a statistical model for describing correlator performance for TV to FLIR correlation, a re-examination has been made of the goodness of the direct correlation estimate for the cross-correlation function.

If we define $s_1(x,y)$ to be the two-dimensional time-frozen image from the reference sensor and $s_2(x,y)$ to be the two-dimensional time-frozen

image from the missile sensor then the cross-correlation function between s_1 and s_2 is given by

$$R_{12}(x_0, y_0, \alpha, \beta) \triangleq E[s_1(x_0, y_0) \, s_2(x_0 + \alpha, y_0 + \beta)] \qquad (18)$$

where $E[\ ]$ implies "expected value of" and since typical imagery is known to be shift-variant, R_{12} depends not only on the relative offset (α, β) between s_1 and s_2 but on the coordinate origin (x_0, y_0) also. Now if we have only one member function for each of s_1 and s_2, without knowing the joint probability density function for s_1 and s_2, R_{12} cannot be computed exactly. Thus, we estimate the value of R_{12} based on K by L samples from s_1 and M by N samples from s_2 to give

$$\hat{R}_{12}(x_0, y_0, p, q) = \frac{1}{KL} \sum_{n=1}^{L} \sum_{m=1}^{K} s_1(n, m) \, s_2(n + p, m + q) \quad (19)$$
$$\text{for} \begin{cases} o \leq p \leq N-L \\ o \leq q \leq M-K \end{cases}$$

where $\hat{R}_{12}$ is an estimate for R_{12}

$$\begin{aligned} x &= n\Delta x & \alpha &= p\Delta x \\ y &= m\Delta y & \beta &= q\Delta y \end{aligned} \qquad (20)$$

Δx, Δy are x and y sample spacing.

If $\hat{R}_{12}$ is to be a good estimate for R_{12} it must be unbiased and consistent.

<u>Unbiased</u>: $E[\hat{R}_{12}] = R_{12}$. $\hat{R}_{12}$ is easily shown to satisfy this requirement and is thus unbiased.

<u>Consistent</u>: $\lim_{KL \to \infty} E[(\hat{R}_{12} - R_{12})^2] = 0.$ \qquad (21)

where the term $E[(\hat{R}_{12} - R_{12})^2]$ is simply the variance of the estimate

about the true value and for a consistent estimate, $\hat{R}_{12}$, the variance goes to zero as the number of data values used in estimating $\hat{R}_{12}$ gets large. Further, the estimate variance is a useful parameter in evaluating the confidence to be placed in a single computation of the cross-correlation $\hat{R}_{12}$. In other words it is relatable to the probability that a given $\hat{R}_{12}$ is within a given error of the true R_{12}.

For the estimate $\hat{R}_{12}$, as defined, consistency is proven for noise-free, distortion-free case below

$$VAR[\hat{R}_{12}] = E[\hat{R}_{12} - R_{12})^2] = E[\hat{R}_{12}^2] - R_{12}^2 \qquad (22)$$

where:
$$E[\hat{R}_{12}^2] = E[(\frac{1}{KL})^2 \sum_{n=1}^{L}\sum_{m=1}^{K}\sum_{i=1}^{L}\sum_{j=1}^{K} s_1(n,m)s_2(n+p, m+q)$$

$$\cdot s_1(i, j)s_2(i+p, j+q)]$$

or using the linearity of $E[\ ]$,

$$E[\hat{R}_{12}^2] = (\frac{1}{KL})^2 \sum_{n=1}^{L}\sum_{m=1}^{K}\sum_{i=1}^{L}\sum_{j=1}^{K} E[s_1(n, m)\ s_2(n+p, m+q)\ s_1(i, j)$$

$$\cdot s_2(i+p, j+q)]$$

Then from [7]

$$E[s_1 s_2 s_3 s_4] = E[s_1 s_2]\ E[s_3 s_4] + E[s_1 s_3]\ E[s_2 s_4] \qquad (23)$$

$$+ E[s_1 s_4]\ E[s_2 s_3] - 2\mu_{s1}\mu_{s2}\mu_{s3}\mu_{s4}$$

and assuming the mean values have been removed, $\mu_{s_i}=0$, all i, we have

$$E[\hat{R}_{12}^2] = (\frac{1}{KL})^2 \sum_{n=1}^{L}\sum_{m=1}^{K}\sum_{i=1}^{L}\sum_{j=1}^{K} R_{12}^2(p, q) + R_{11}(i-n, j-m)$$
$$\qquad (24)$$

$$\cdot R_{22}(i-n, j-m) + R_{12}(i+p-n, j+q-m)R_{21}(i-p-n, j-q-m)$$

where R_{11} and R_{22} are the autocorrelation functions for s_1 and s_2 respectively and R_{21} and R_{12} are cross correlation functions for s_1 and s_2.

The R_{ij} terms obtained are exact functions; further $R_{12}{}^2(p, q)$ is independent of the summation indices. Using this result, the $\text{VAR}[\hat{R}_{12}]$ becomes

$$\sigma_{\hat{R}_{12}}^2 = \text{VAR}[R_{12}(x_0, y_0, p, q)] = \left(\frac{1}{KL}\right)^2 \sum_{\ell=-(L-1)}^{L-1} \sum_{k=-(K-1)}^{K-1} (L-|\ell|)(K-|k|)$$

$$\cdot \{R_{11}(\ell, k)R_{22}(\ell, k) + R_{12}(\ell+p, k+q)R_{21}(\ell-p, k-q)\} \quad (25)$$

$$\sigma_{\hat{R}_{12}}^2 = \frac{1}{KL} \sum_{\ell=-(L-1)}^{L-1} \sum_{k=-(K-1)}^{K-1} \left(1-\frac{|\ell|}{L}\right)\left(1-\frac{|k|}{K}\right)\{R_{11}(\ell, k)R_{22}(\ell, k)$$
$$+ R_{12}(\ell+p, k+q)R_{21}(\ell-p, k-q)\} \quad (26)$$

where the following changes of variables have been made

$$\ell=i-n \quad ; \quad -(L-1) \le \ell \le (L-1)$$
$$k=j-m \quad ; \quad -(K-1) \le k \le (K-1) \quad (27)$$

and the $L-|\ell|$, $K-|k|$ terms arise because for each value of ℓ & k there are $(L-|\ell|)(K-|k|)$ identical terms under the quad sum.

If

$$\sum_{\ell}\sum_{k}\{R_{11}(\ell, k)R_{22}(\ell, k) + R_{12}(\ell+p, k+q)R_{21}(\ell-p, k-q) < \infty$$

for all x_0, y_0, p and q then clearly $\lim_{KL \to \infty} \sigma_{\hat{R}_{12}}^2 = 0$ and $\hat{R}_{12}$ is a consistent estimate of the true cross correlation function R_{12}.

Of further significance is that $\sigma_{\hat{R}_{12}}^2$ shows how the variance

(and thus reliability, confidence interval, error probability) depends
on not only the coordinate origin (x_0, y_0) but on individual shift
values within a given correlation surface estimate. Dependence on scene
statistics is inherent in the R_{11} & R_{22} terms in the variance.

The above development formalizes the statistical approach to error
probability and registration probability for the noise-free distortion-free
cross-correlation function estimate. Noise is easily included by replac-
ing s_1 and s_2 with $s_1 + n_1$ and $s_2 + n_2$ respectively. Similar results are
expected.

2. Correct Registration

The following development is an extension of the work in [7] to include
the situation where, at registration, there are pixel mis-matches between
the two images (in the absence of noise). These pixel mis-matches may be
caused by contrast reversals between the TV and FLIR sensors or may be
caused by image distortion. The effect of these mis-matches is incorpora-
ted into the model in [7] by the parameter, ϵ, which is defined to be the
probability that a FLIR and TV pixel do not match, given that the images
are registered. There is, unfortunately, still a problem in determining
a realistic value for ϵ since it will be scene dependent.

The assumption that all pixels are independent as used in [7] is still
employed in this analysis. This assumption has its greatest validity for
scenes with high spatial frequency content such that oversampling is not
evident. For scenes with larger objects (lower spatial frequencies),
considerable oversampling is evident and the assumption of independent
pixels begins to break down. The result is a broader peak in the

cross-correlation function and, hence, further confusion on choice of a suitable threshold for correlation peak detection.

At registration, because of contrast reversals and distortion, the new model for probability of correct registration has the following features:

1. Pixel values $\mu_1(n, m)$ and $\mu_2(n+p_0, m+q_0)$ are not necessarily equal and have a probability of mismatch $= \epsilon$.

2. Array averages T_1 and T_2 are not necessarily equal.

3. The pixel mismatch probability, ϵ, is exclusive of noise induced mismatch.

Thus, for the n, mth pixel pair comparison at registration we have

$$r_1(n, m) = \mu_1(n, m) + n_1(n,m)$$

$$r_2(m+p_0, m+q_0) = \mu_2(n+p_0, m+q_0) + n_2(n+p_0, m+q_0)$$

where the noise terms n_1 and n_2 are signal fluctuations due to both optical and electronic causes and are assumed to be zero-mean gaussian.

Then for the n, mth pixel pair

$$
\begin{aligned}
P_{n,m}[C] &= P[\text{pixels match/images registered}] \\
&= P[g_1(r_1) = 0 \ \& \ g_2(r_2) = 0] \\
&\quad + P[g_1(r_1) = 1 \ \& \ g_2(r_2) = 1]
\end{aligned}
\tag{28}
$$

or equivalently, looking at all possible combinations for which the pixels match, we get

$$
\begin{aligned}
P_{n,m}[C] &= P[r_1 < T_1 \ \& \ r_2 < T_2 | \mu_1 < T_1 \ \& \ \mu_2 < T_2] \ P[\mu_1 < T_1 \ \& \ \mu_2 < T_2] \\
&\quad + P[r_1 < T_1 \ \& \ r_2 < T_2 | \mu_1 < T_1 \ \& \ \mu_2 < T_2] \ P[\mu_1 < T_1 \ \& \ \mu_2 < T_2]
\end{aligned}
\tag{29}
$$

$$+P[r_1>T_1 \ \& \ r_2>T_2|\mu_1>T_1 \ \& \ \mu_2>T_2] \ P[\mu_1>T_1 \ \& \ \mu_2>T_2]$$

$$+P[r_1>T_1 \ \& \ r_2>T_2|\mu_1<T_1 \ \& \ \mu_2<T_2] \ P[\mu_1<T_1 \ \& \ \mu_2<T_2]$$

$$+P[r_1<T_1 \ \& \ r_2<T_2|\mu_1<T_1 \ \& \ \mu_2>T_2] \ P[\mu_1<T_1 \ \& \ \mu_2>T_2]$$

$$+P[r_1<T_1 \ \& \ r_2<T_2|\mu_1>T_1 \ \& \ \mu_2<T_2] \ P[\mu_1>T_1 \ \& \ \mu_2<T_2]$$

$$+P[r_1>T_1 \ \& \ r_2>T_2|\mu_1>T_1 \ \& \ \mu_2<T_2] \ P[\mu_1>T_1 \ \& \ \mu_2<T_2]$$

$$+P[r_1>T_1 \ \& \ r_2>T_2|\mu_1<T_1 \ \& \ \mu_2>T_2] \ P[\mu_1<T_1 \ \& \ \mu_2>T_2]$$

Or looking at the domain of values for r_1 and r_2 we see four areas delinea-ted by lines through the quantization thresholds T_1 & T_2.   Then in terms
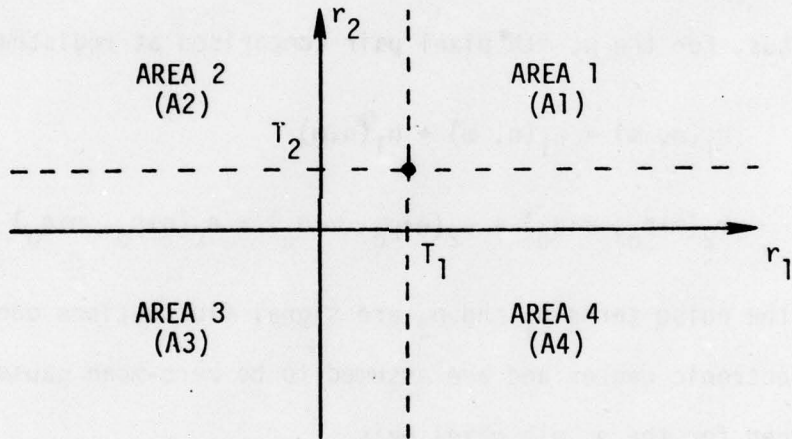

Figure 42.   Domain of values for r_1 and r_2.

of these areas and the probability density functions for n_1 and n_2 we get

$$P_{n,m}[C] = \iint_{A3} P_{n1}(r_1-\mu_1) \ P_{n2}(r_2-\mu_2) \Bigg|_{r_1, \ r_2 \ in \ A3} \cdot P[r_1, \ r_2 \ in \ A3]$$
$$+ \iint_{A3} P_{n1}(r_1-\mu_1) \ P_{n2}(r_2-\mu_2) \Bigg|_{r_1, \ r_2 \ in \ A1} \cdot P[r_1, \ r_2 \ in \ A1] \tag{30}$$

$$+ \iint_{A1} P_{n1}(r_1-\mu_1) \; P_{n2}(r_2-\mu_2) \Big|_{r_1, \; r_2 \; in \; A1} \cdot P[r_1, \; r_2 \; in \; A1] \left. \begin{array}{c} \\ \end{array} \right\} \begin{array}{l} \text{Pixels} \\ \text{Match} \end{array}$$

$$+ \iint_{A1} P_{n1}(r_1-\mu_1) \; P_{n2}(r_2-\mu_2) \Big|_{r_1, \; r_2 \; in \; A3} \cdot P[r_1, \; r_2 \; in \; A3]$$

$$+ \iint_{A3} P_{n1}(r_1-\mu_1) \; P_{n2}(r_2-\mu_2) \Big|_{r_1, \; r_2 \; in \; A2} \cdot P[r_1, \; r_2 \; in \; A2]$$

$$+ \iint_{A3} P_{n1}(r_1-\mu_1) \; P_{n2}(r_2-\mu_2) \Big|_{r_1, \; r_2 \; in \; A4} \cdot P[r_1, \; r_2 \; in \; A4] \left. \begin{array}{c} \\ \\ \\ \\ \end{array} \right\} \begin{array}{l} \text{Pixels} \\ \text{Mismatch} \end{array}$$

$$+ \iint_{A1} P_{n1}(r_1-\mu_1) \; P_{n2}(r_2-\mu_2) \Big|_{r_1, \; r_2 \; in \; A4} \cdot P[r_1, \; r_2 \; in \; A4]$$

$$+ \iint_{A1} P_{n1}(r_1-\mu_1) \; P_{n2}(r_2-\mu_2) \Big|_{r_1, \; r_2 \; in \; A2} \cdot P[r_1, \; r_2 \; in \; A2]$$

From the symmetry of the above expression and recognizing that

$$P[r_1, \; r_2 \; in \; A2] + P[r_1, \; r_2 \; in \; A4] = \epsilon$$

$$P[r_1, \; r_2 \; in \; A1] + P[r_1, \; r_2 \; in \; A3] = 1 - \epsilon \quad ; \tag{31}$$

further if we define signal-to-noise ratios for the two signals as

$$SN1 \triangleq \frac{|\mu_1(n,m) - T_1|}{\sigma_{n1}}$$

$$SN2 \triangleq \frac{|\mu_2(n+p_o, \; m+q_o) - T_2|}{\sigma_{n2}} \tag{32}$$

i.e., SN1 and SN2 are always positive and held at constant values for

r_1, r_2 in A1, A2, A3 or A4, then

$$P_{n,m}[C] = \{ \int_{-\infty}^{T} \int_{-\infty}^{T} P_{n1}(r_1-\mu_1) \, P_{n2}(r_2-\mu_2) \} \quad P[A3]: \mu_1 < T_1; \; \mu_2 < T_2$$

$$+ \{ \int_{-\infty}^{T} \int_{-\infty}^{T} P_{n1}(r_1-\mu_1) \, P_{n2}(r_2-\mu_2) \} \quad P[A1]: \mu_1 > T_1; \; \mu_2 > T_2$$

$$+ \{ \int_{T}^{\infty} \int_{T}^{\infty} P_{n1}(r_1-\mu_1) \, P_{n2}(r_2-\mu_2) \} \quad P[A1]: \mu_1 > T_1; \; \mu_2 > T_2$$

$$+ \{ \int_{T}^{\infty} \int_{T}^{\infty} P_{n1}(r_1-\mu_1) \, P_{n2}(r_2-\mu_2) \} \quad P[A3]: \mu_1 < T_1; \; \mu_2 < T_2$$

$$\text{(33)}$$

$$+ \{ \int_{-\infty}^{T} \int_{-\infty}^{T} P_{n1}(r_1-\mu_1) \, P_{n2}(r_2-\mu_2) \} \quad P[A2]: \mu_1 < T_1; \; \mu_2 > T_2$$

$$+ \{ \int_{-\infty}^{T} \int_{-\infty}^{T} P_{n1}(r_1-\mu_1) \, P_{n2}(r_2-\mu_2) \} \quad P[A4]: \mu_1 > T_1; \; \mu_2 < T_2$$

$$+ \{ \int_{T}^{\infty} \int_{T}^{\infty} P_{n1}(r_1-\mu_1) \, P_{n2}(r_2-\mu_2) \} \quad P[A4]: \mu_1 > T_1; \; \mu_2 < T_2$$

$$+ \{ \int_{T}^{\infty} \int_{T}^{\infty} P_{n1}(r_1-\mu_1) \, P_{n2}(r_2-\mu_2) \} \quad P[A2]: \mu_1 < T_1; \; \mu_2 > T_2$$

which is simplified using the following. In the above, we need to evaluate

$$\left. \begin{array}{l} \int_{-\infty}^{T} \frac{1}{\sqrt{2\pi}} \, e^{\frac{-(r-\mu)^2}{2\sigma^2}} \, dr \\[4mm] \text{and} \quad \int_{T}^{\infty} \frac{1}{\sqrt{2\pi}} \, e^{\frac{-(r-\mu)^2}{2\sigma^2}} \, dr \end{array} \right\} \qquad \text{(34)}$$

Making a change of variable

$$
\left.\begin{aligned}
\frac{r-\mu}{\sigma} &= \alpha \\[1em]
d\alpha &= \frac{dr}{\sigma}
\end{aligned}\right\}
\qquad
\left.\begin{aligned}
r &\to T \\[1em]
\alpha &\to \frac{T-\mu}{\sigma}
\end{aligned}\right\}
\tag{35}
$$

We have

$$
\left.\begin{aligned}
\int_{-\infty}^{SN} \frac{1}{\sqrt{2\pi}}\, e^{-\frac{\alpha^2}{2}}\, d\alpha \\[2em]
\int_{SN}^{\infty} \frac{1}{\sqrt{2\pi}}\, e^{-\frac{\alpha^2}{2}}\, d\alpha
\end{aligned}\right\}
\quad \text{for } T > \mu
$$

and

$$
\left.\begin{aligned}
\int_{-\infty}^{-SN} \cdot \frac{1}{\sqrt{2\pi}}\, e^{-\frac{\alpha^2}{2}}\, d\alpha \\[2em]
\int_{-SN}^{\infty} \frac{1}{\sqrt{2\pi}}\, e^{-\frac{\alpha^2}{2}}\, d\alpha
\end{aligned}\right\}
\quad \text{for } \mu > T
\tag{36}
$$

Then we get

$$
\begin{aligned}
P_{n,m}[C] = P[A3] &\int_{-\infty}^{SN1} \int_{-\infty}^{SN2} \frac{1}{2\pi}\, e^{-\frac{(\alpha^2 + \beta^2)}{2}}\, d\alpha\, d\beta \\[1.5em]
\div P[A1] &\int_{-\infty}^{-SN1} \int_{-\infty}^{SN2} \frac{1}{2\pi}\, e^{-\frac{(\alpha^2 + \beta^2)}{2}}\, d\alpha\, d\beta \\[1.5em]
+ P[A1] &\int_{-SN1}^{\infty} \int_{-SN2}^{\infty} \frac{1}{2\pi}\, e^{-\frac{(\alpha^2 + \beta^2)}{2}}\, d\alpha\, d\beta
\end{aligned}
\tag{37}
$$

$$+ P[A3] \int_{SN1}^{\infty} \int_{SN2}^{\infty} \frac{1}{2\pi} e^{-\frac{(\alpha^2 + \beta^2)}{2}} d\alpha d\beta$$

$$+ P[A2] \int_{-\infty}^{SN1} \int_{-\infty}^{-SN2} \frac{1}{2\pi} e^{-\frac{(\alpha^2 + \beta^2)}{2}} d\alpha d\beta$$

$$+ P[A4] \int_{-\infty}^{-SN1} \int_{-\infty}^{SN2} \frac{1}{2\pi} e^{-\frac{(\alpha^2 + \beta^2)}{2}} d\alpha d\beta$$

$$+ P[A4] \int_{-SN1}^{\infty} \int_{SN2}^{\infty} \frac{1}{2\pi} e^{-\frac{(\alpha^2 + \beta^2)}{2}} d\alpha d\beta$$

$$+ P[A2] \int_{SN1}^{\infty} \int_{SN2}^{\infty} \frac{1}{2\pi} e^{-\frac{(\alpha^2 + \beta^2)}{2}} d\alpha d\beta$$

Now making use of the following

$$1 - \int_{-A}^{\infty} = \int_{-\infty}^{-A} = 1 - \int_{-\infty}^{A} = \int_{A}^{\infty} \quad \Bigg\} \tag{38}$$

$$\int_{-\infty}^{A} = \frac{1}{2} + erf(A)$$

where $erf(A) \triangleq \int_{0}^{A} \frac{1}{\sqrt{2\pi}} e^{-\frac{\alpha^2}{2}} d\alpha$

then

$$P_{n,m}[C] = P[A3] \{[\tfrac{1}{2}+erf(SN1)][\tfrac{1}{2}+erf(SN2)] + [\tfrac{1}{2}-erf(SN1)][\tfrac{1}{2}-erf(SN2)]\}$$
$$+ P[A1] \{[\tfrac{1}{2}-erf(SN1)][\tfrac{1}{2}-erf(SN2)] + [\tfrac{1}{2}+erf(SN1)][\tfrac{1}{2}+erf(SN2)]\}$$
$$+ P[A2] \{[\tfrac{1}{2}+erf(SN1)][\tfrac{1}{2}-erf(SN2)] + [\tfrac{1}{2}-erf(SN1)][\tfrac{1}{2}+erf(SN2)]\}$$
$$+ P[A4] \{[\tfrac{1}{2}-erf(SN1)][\tfrac{1}{2}+erf(SN2)] + [\tfrac{1}{2}+erf(SN1)][\tfrac{1}{2}-erf(SN2)]\}$$

or

$$P_{n,m}[C] = (1 - \epsilon) \{\tfrac{1}{2} + 2\, erf(SN1)\, erf(SN2)\}$$
$$+ \quad \epsilon \quad \{\tfrac{1}{2} - 2\, erf(SN1)\, erf(SN2)\} \tag{39}$$

or finally

$$P_{n,m} [C] = \frac{1}{2} + 2erf(SN1) \; erf(SN2) - 4\epsilon erf(SN1) \; erf(SN2)$$

(40)

$$P_{n,m} [C] = \frac{1}{2} + 2(1-\epsilon)[erf(SN1) \; erf(SN2)]$$

This result is interesting in that we have derived in a cumbersome, brute-force manner what should be intuitively obvious. That is, this result differs from the case of no pixel mis-matches only in inclusion of the $(1-\epsilon)$ term, which is simply the probability that pixels match between the TV and FLIR. And since the pixel match probability and the probability of choosing pixels matched are independent of each other, the simple multi-plication result was expected.

It is emphasized again that SN1 and SN2 are different for each pixel pair in the correlation function computation so that for KL pixel compari-sons one can talk about expected values for $P_{n,m} [C]$. To compute $\bar{p} = E[P_{n,m} [C]]$ requires knowledge of the image statistics for μ_1 and μ_2 as well as knowledge of noise variances.

An approach similar to that given in [7] where assumed scene statistics are used can again be applied and carried through to a detection probability for given thresholds. The effect of ϵ on these quantities will be a general reduction in $\bar{p}$ and thus a reduction in P_D for any given threshold.

5. CONCLUSIONS AND RECOMMENDATIONS

Most of the conclusions and recommendations resulting from the work on this contract have been given and justified within the first four chapters of this report. For compactness they are given again in this chapter.

1. In order for the correlation of binary images to be a valid measure of similarity it is necessary that the quantization process be based on similar measures of scene content. For sensors operating in different frequency spectrums, quantization based on average value or standard deviation do not supply similar binary images to the correlation system. Quantization based on edge content overcomes this limitation.

2. In support of the results outlined in [4], the correlation system simulations performed under this contract show that TV-to-TV correlations work well when quantization is based on a line average or array average threshold. The simulations indicate that the above threshold technique which yields the best result (sharpest correlation peak) is scene dependent.

3. From the set of simulations conducted for TV-to-IR correlations using the average value preprocessors no valid correlations were found. It is unlikely that these preprocessors, acting alone, would be able to provide valid and reliable correlations when the sensors are non-compatible.

4. From the set of simulations conducted for TV-to-IR correlation using

111

the standard deviation preprocessors no valid correlations were found. However, there are factors, not studied thoroughly in this effort, which could effect the outcome of the correlation system. The effects of factors such as: 1. average value and standard deviation calculation sample size, 2. proportionality constant, K, chosen for $K\sigma$ quantization threshold, and 3. reference image size should be studied more thoroughly before these preprocessors are eliminated for TV-to-IR correlation.

5. The poor performance of the average value and standard deviation preprocessors in the correlation system for TV-to-IR correlation led to the use of the edge detector preprocessors.

6. The one/zero distribution in the reference image directly effects the quality of the correlation function when using edge content quantization for TV-to-IR correlation. The most successful correlations were achieved with an equal one/zero reference image distribution. It is recommended that the gradient threshold for the reference image be set at the median gradient value of the HR-TV image.

7. From the set of simulations conducted for TV-to-IR correlations using the edge detector preprocessors it is felt that the 3 x 3 edge detection algorithm produces correlation results that are more reliable than those produced using the 2 x 2 edge detector.

8. Contract personnel are aware of one LSI chip which accomplishes the function of a Sobel edge detector (3 x 3 detector). It is recommended that this chip or a similar chip be used in a hardware implementation of an edge detection preprocessing algorithm.

9. The simple edge detection algorithms studied via simulation did lead to correct correlation most of the time. Other, more elaborate, edge detection systems would probably lead to a more reliable correlation function, at the cost of slower computational time and increased hardware mainly in memory. These algorithms were not seriously considered in this study, because of the requirement to integrate the recommendation into an existing correlator. It is recommended that additional study be conducted to investigate more elaborate preprocessing algorithms.

10. The proper selection of gradient threshold in the edge detector preprocessors for both the PTS and sensor image is critical. Item 6 above outlines a method of threshold selection for the PTS image. Adjustment of the threshold for the sensor image could be done over 3 or 4 successive fields to select the one which gives the best results. Additional study should be conducted for gradient threshold selection for the sensor image using a larger data base.

11. Proper PTS image resolution reduction for both TV-to-TV and TV-to-IR correlations is critical. Incorrect calculation of both the horizontal and vertical scale factors severely degrade the correlator's performance.

12. The dynamic response of the IR sensors limit the sampling rate used for the IR video. Calculations made and simulations support the fact that an equivalent sampling of 2.5 MHz is optimum.

REFERENCES

1. R. O. Duda and P. E. Hart, Pattern Classification and Scene Analysis, pp. 268-272, John Wiley and Sons, New York, 1973.

2. WERNER FREI and Chung-Ching Chen, "Fast Boundary Detection: A Generalization and a New Algorithm," IEEE Transactions on Computers, Vol. C-26 No. 10, pp. 988-998, October 1977.

3. Guner S. Robinson, "Detection and Coding of Edges Using Directional Masks," Optical Engineering, Vol. 16 No. 6, pp. 580-585, November - December 1977.

4. J. S. Boland, III, L. J. Pinson, G. R. Kane, M. A. Honnell, and E. G. Peters, "Automatic Target Hand-Off Using Correlation Techniques," Final Technical Report Contract DAAH01-76-C-0396, 31 January 1977.

5. W. W. Malcolm, and J. S. Boland, III, "Preliminary Analysis of Automatic Scene Correlation Between Spectrially Non-Compatable Imagery," TR-TG-78-85, G & C Directorate, Tech Lab, MIRADCOM, Redstone Arsenal, Alabama, September 1978.

6. L. J. Pinson, J. S. Boland, III, and W. W. Malcolm, "Statistical Analysis for a Binary Image Correlator in the Absence of Geometric Distortion," To appear in Optical Engineering.

7. Bendat and Piersol, Random Data: Analysis and Measurement Procedures, Wiley, 1971, p. 92 for Gaussian random processes and p. 182 for argument for extension to non-gaussian random processes.